

Metal-insulator transition and robust thermoelectricity via strain-tuned interplay between structural and electronic properties in $(\text{SrVO}_3)_1/(\text{SrTiO}_3)_1(001)$ superlattices

Manish Verma and Rossitza Pentcheva 

Department of Physics and Center for Nanointegration (CENIDE), Universität Duisburg-Essen, Lotharstr. 1, 47057 Duisburg, Germany



(Received 31 October 2021; revised 12 April 2022; accepted 3 June 2022; published 7 July 2022)

Exploring the origin of the metal-to-insulator transition (MIT) in transition metal oxide heterostructures is of high interest in current condensed matter physics research. Here based on density functional theory calculations with the meta-GGA exchange correlation functional SCAN, we find distinct mechanisms of MIT in $(\text{SrVO}_3)_1/(\text{SrTiO}_3)_1(001)$ superlattices (SLs). The SCAN functional is sufficient to determine the ground state structure and possible symmetry breaking at a given lateral lattice constant and best describes the electronic and magnetic properties of the weakly correlated $(\text{SrRuO}_3)_1/(\text{SrTiO}_3)_1(001)$ SL and its constituents by minimizing the self-interaction error. However, an additional Hubbard U term is necessary for the strongly correlated $(\text{SrVO}_3)_1/(\text{SrTiO}_3)_1(001)$ SLs. We show that SCAN + U always favors the monoclinic ($P2_1/c$) symmetry in $(\text{SrXO}_3)_1/(\text{SrTiO}_3)_1(001)$ SLs, $X = \text{V}$ and Ru , irrespective of the in-plane lattice constant and X . For the orthorhombic $(\text{SrVO}_3)_1/(\text{SrTiO}_3)_1(001)$ SL ($Cmmm$) at a_{STO} (tensile strain +1.7%), we report strong correlation and confinement driven Mott-Hubbard type MIT via long-range stripe antiferromagnetic ordering, whereas, under compressive strain (−3.6%) at a_{YAO} , the interplay of confinement, correlation, and finite octahedral tilts and rotations lead to monoclinic ($P2_1/c$) symmetry, which drives an orbital reconstruction and a concomitant MIT with ferromagnetic spin alignment. Lastly, using Boltzmann transport theory within the constant relaxation time approximation, for $(\text{SrVO}_3)_1/(\text{SrTiO}_3)_1(001)$ SL at a_{STO} , we obtain large n -type Seebeck coefficients S of −566 (in-plane) and −454 $\mu\text{V}/\text{K}$ (cross-plane), respectively, along with an in-plane (cross-plane) power factor of 31.4 (8.5) $\mu\text{W K}^{-2} \text{cm}^{-1}$ (assuming $\tau = 4$ fs) at 300 K. These values directly categorize $(\text{SrVO}_3)_1/(\text{SrTiO}_3)_1(001)$ SL as a promising oxide thermoelectric material.

DOI: [10.1103/PhysRevResearch.4.033013](https://doi.org/10.1103/PhysRevResearch.4.033013)

I. INTRODUCTION

Identifying the mechanism behind the metal-to-insulator transition (MIT) in strongly correlated transition metal oxides (TMO) heterostructures at the ultrathin limit is one central problem in condensed matter physics. Achieving such an ultrathin limit became viable due to the ability to synthesize TMO heterostructures with atomically sharp interfaces [1]. Low dimensional strongly correlated electron systems are susceptible to collective ordering phenomena resulting in spin- and charge-ordered phases different from the bulk [2].

SrVO_3 (SVO) ($S = 1/2$, d^1), albeit paramagnetic metal in the bulk, is a model strongly correlated system for the study of various mechanisms of MIT and possible spin ordering at the ultrathin limit [3,4]. Yoshimatsu *et al.* [5] reported *in situ* photoemission spectra of ultrathin SVO films, showing the evolution of electronic structure. They found a Mott-Hubbard band gap opening in the vicinity of the Fermi level for a film thickness below 2–3 unit cells (u.c.), triggered by a bandwidth reduction due to the dimensional crossover from 3D to 2D.

Further studies also revealed the dimensional crossover MIT of SVO ultrathin films by *ex situ* transport measurements: The MIT occurred at 200 K for films grown with a thickness of 3 nm [6], while Fouchet *et al.* [7] found insulating behavior in the temperature range from 2 to 300 K for a film with a thickness of 2 nm. More recently, Wang *et al.* [8] experimentally reported the dominant role of electron-electron interactions in the dimensional crossover MIT in SVO thin films as well as in $\text{SrVO}_3/\text{SrTiO}_3(001)$ superlattices (SLs). On the other hand, Pardo *et al.* [9] showed a spin-orbit coupling (SOC) driven ferromagnetic (FM) Mott-insulating phase in confined SVO slabs.

In solids having partially occupied degenerate levels, the Jahn-Teller effect occurs when the lattice distorts coherently so as to lift orbital degeneracy. For example, YVO_3 is a typical Mott-Hubbard type insulator that undergoes magnetic ($T_N < 115$ K) and structural ($T < 71$ K) transitions, accompanied by spin and orbital orderings, respectively [10–12]. Below the structural transition temperature, the Jahn-Teller effect results in distortion of the VO_6 octahedra leading to C-type orbital-ordering accompanied by alternating occupation of $d_{xy}^1 d_{yz}^1 / d_{xy}^1 d_{xz}^1$ orbitals along with the G-type antiferromagnetic (AFM) spin ordering [13]. Similarly, in a recent work on $(\text{SrVO}_3)_1/(\text{SrTiO}_3)_1(001)$ SL ($(\text{SVO})_1/(\text{STO})_1(001)$) [14], MIT was driven by octahedral tilts and rotations. This results in a monoclinic ($P2_1/c$) symmetry, accompanied by an orbital reconstruction leading

Published by the American Physical Society under the terms of the Creative Commons Attribution 4.0 International license. Further distribution of this work must maintain attribution to the author(s) and the published article's title, journal citation, and DOI.

to an alternating occupation of d_{xz}/d_{yz} orbitals at neighboring V sites. This indicates that spatial symmetry breaking (achieved via octahedral tilts and rotations) favors Mott-type MIT. Similar insulating states due to symmetry breaking were first reported in $(\text{SrFeO}_3)_1/(\text{SrTiO}_3)_1(001)$ SL [15,16].

However, in modeling such Mott-Hubbard insulators, Varignon *et al.* [17] argued that the calculations performed within density functional theory (DFT) [18] or DFT + U [19], by adopting low-temperature experimental structures, do not prove the dominant role of electronic correlations over structural symmetry-breaking modes, resulting in MIT. Instead, in Mott-Hubbard theory [20–22], the band gap in the AFM and paramagnetic (PM) phases of $3d$ oxides with partially occupied degenerate orbitals emerges solely due to strong correlation without spatial symmetry breaking. Still, the spatial symmetry can break afterward but is not a prerequisite for MIT. Hence, the MIT in $(\text{SVO})_1/(\text{STO})_1(001)$ SL, achieved by allowing the octahedral tilts and rotations [14], tends to put the structural distortions on a similar footing with strong correlations, undermining the dominant role of the latter.

Furthermore, a recent DFT + DMFT study explored the possibility of ordered phases or long-range fluctuations in SVO monolayer (ultrathin film), deposited on a STO substrate [23]. Adopting a tetragonal structure, they obtained a Mott-insulating phase with G-type AFM order, involving only d_{xy} occupied orbital in the stoichiometric SrO terminated SVO thin film, proving the dominant role of strong correlations behind the Mott-Hubbard type MIT. If the $(\text{SVO})_1/(\text{STO})_1(001)$ SL structure is constrained to tetragonal ($P4/mmm$) symmetry, breathing mode distortion (charge disproportionation or charge ordering) opens a band gap [14]. However, the charge-ordering gains importance if the system is close to MIT [24]. In addition, another recent experimental study on SVO thin films showed that the t_{2g} orbitals hierarchy is modified by epitaxial strain [25], which are otherwise degenerate in the SVO bulk. They found that the $3d_{xy}$ orbital is preferentially occupied by the electrons at tensile strain (a_{STO}), distinct from $3d_{xz}/d_{yz}$ orbital occupation at compressive strain (a_{LAO}). This further tends to contradict the previous report of orbital ordering involving the occupation of $3d_{xz}/d_{yz}$ orbitals as the possible mechanism for MIT in $(\text{SVO})_1/(\text{STO})_1(001)$ SL at a_{STO} . Hence it is imperative to ask whether DFT + U can demonstrate the strong correlation driven MIT in $(\text{SVO})_1/(\text{STO})_1(001)$ SL, i.e., without allowing octahedral rotations and tilts? Secondly, what kind of magnetic order will sustain in the case of ultrathin vanadate SL, compared to ultrathin film?

Lastly, Katsufuji *et al.* [26] recently reported a large interfacial thermal resistance in $(\text{SVO})/(\text{STO})(001)$ multilayer thin films despite the similar phononic properties of the constituent bulk compounds, making it suitable for thermoelectric applications. This motivated us to revisit the thermoelectric properties, especially to obtain realistic estimate for the total figure of merit ($ZT|_{\text{tot}}$) by including the thermal conductivity obtained from experiment, beyond the previous report [14].

This paper is organized as follows. Section II discusses the computational details employed in this work. Section III addresses the effect of GGA (PBEsol [27]) versus meta-GGA (SCAN [28]) exchange-correlation functional as well

as the influence of a Hubbard U parameter on the ground state properties of the weakly correlated bulk SrRuO_3 and $(\text{SrRuO}_3)_1/(\text{SrTiO}_3)_1(001)$ SL. Section IV assesses the strong correlation in bulk SrVO_3 where the Hubbard U parameter in bulk SrVO_3 is determined using the linear response approach. The effect of Hubbard U parameter with the SCAN and PBEsol exchange-correlation functionals on the t_{2g} bandwidth of bulk SrVO_3 is explored. Section V points out that SCAN + U always favors the monoclinic ($P2_1/c$) symmetry in $(\text{SrXO}_3)_1/(\text{SrTiO}_3)_1(001)$ SLs, $X = \text{V}$, and Ru, irrespective of in-plane lattice constant and X . The ground state structural symmetry of $(\text{SrVO}_3)_1/(\text{SrTiO}_3)_1(001)$ SLs at the lateral lattice constants of SrTiO_3 and YAlO_3 , respectively, is determined using the SCAN functional. Lastly, a general recipe is outlined to determine the correct ground state structural symmetry and electronic properties while addressing the strong correlation effects in $(\text{SrXO}_3)_1/(\text{SrTiO}_3)_1(001)$ SLs, X being a transition metal cation. Subsequently, Secs. VI and VII present the electronic and magnetic properties of $(\text{SrVO}_3)_1/(\text{SrTiO}_3)_1(001)$ SL at the lateral lattice constant of SrTiO_3 and YAlO_3 , respectively, using the correct structural symmetries determined by the SCAN functional in Sec. V. Lastly, Sec. VIII presents the thermoelectric properties of $(\text{SrVO}_3)_1/(\text{SrTiO}_3)_1(001)$ SL at the lateral lattice constant of SrTiO_3 using Boltzmann transport theory within the constant relaxation time approximation.

II. COMPUTATIONAL DETAILS

First-principles calculations for $(\text{SrXO}_3)_1/(\text{SrTiO}_3)_1(001)$ SLs, $X = \text{V}$, Ru, and their respective bulk phases were performed within the framework of spin-polarized DFT [18]. The calculations were carried out using the Vienna *ab initio* simulation package (VASP) [29,30] along with the projector augmented wave (PAW) basis [31,32]. To determine the ground state symmetry at a given lattice constant, and to calculate the electronic and magnetic properties of $(\text{SrXO}_3)_1/(\text{SrTiO}_3)_1(001)$ SLs, $X = \text{V}$, Ru, and their respective bulk phases, metaGGA SCAN [28] was employed as the exchange-correlation functional. In order to take static correlation into account in $(\text{SrVO}_3)_1/(\text{SrTiO}_3)_1(001)$ SL, $U = 2$ and 3 eV, respectively, were used at the V- $3d$ sites in combination with the SCAN exchange-correlation functional. Moreover, we calculated the electronic and magnetic properties of bulk SrRuO_3 , bulk SrTiO_3 , and $(\text{SrRuO}_3)_1/(\text{SrTiO}_3)_1(001)$ SL using both SCAN and PBEsol, as well as taking into account the effect of an additional U parameter ($U = 1$ and 2 eV at Ru $4d$ and Ti $3d$ states, respectively). The effect of Hubbard U parameter on the structural properties of $(\text{SrRuO}_3)_1/(\text{SrTiO}_3)_1(001)$ SLs was explored via PBEsol + U ($U = 3$ eV at Ru $4d$ and 2 eV at Ti $3d$) and SCAN + U ($U = 2$ eV at Ru $4d$) calculations, respectively. Similarly, to understand the effect of the Hubbard U term on structural properties of bulk SrRuO_3 and SrTiO_3 , additional calculations were performed using SCAN+ U ($U = 1$ and 2 eV at Ru $4d$ and 2 eV at Ti $3d$ states, respectively). Furthermore, spin-orbit coupling (SOC) was included for bulk SrRuO_3 and $(\text{SrRuO}_3)_1/(\text{SrTiO}_3)_1(001)$ SL to calculate the magneto-crystalline anisotropy energies (MAE).

To allow spatial-symmetry breaking, and to explore different magnetic configurations, we adopt a $2\sqrt{2}a \times 2\sqrt{2}a \times 2c$ supercell (80 atoms), rotated by 45° about the [001] axis with respect to the cubic perovskite unit cell, having the lattice parameter a , compared to the previously used $\sqrt{2}a \times \sqrt{2}a \times 2c$ SL (20 atoms) [14–16]. The in-plane lattice constant of the 1/1 SLs was fixed to the experimental lattice constants of bulk STO, $a = 3.905 \text{ \AA}$, and bulk YAlO₃ (YAO), $a = 3.708 \text{ \AA}$, respectively, while the c parameter along with the internal positions were fully optimized, until the forces were less than 0.01 eV/\AA . To sample the Brillouin-zone, we have used $8 \times 8 \times 6$ and $4 \times 4 \times 6$ Monkhorst-pack k -point grids [33] for the bulk SRO (STO) and 1/1 SLs, respectively. The cutoff energy of 500 eV was used for the basis set in all the calculations.

Next, the BOLTZTRAP code [34] was employed to provide the energy- and spin-resolved transmission $T_\sigma(E)$ from the DFT + U electronic structure by using Boltzmann transport theory in the constant relaxation time approximation. We obtained converged transmission curves for $16 \times 16 \times 24$ k points for the SLs. Subsequently, we calculated the thermoelectric quantities by using the approach of Sivan and Imry [35], which has been described in detail elsewhere [36–43].

Lastly, additional calculations were performed to determine the Hubbard U parameter for bulk SrVO₃ using linear response theory as implemented in the plane wave (PW) pseudopotential QUANTUM ESPRESSO code [44–46]. PBEsol exchange-correlation functional along with PAW type pseudopotentials were used [47]. Kohn-Sham wavefunctions and charge density were expanded in plane-waves up to energy cutoffs of 60 and 700 Ry, respectively. A Γ -centered k mesh of $8 \times 8 \times 8$ was used in all the calculations. DFT + U calculations were performed using the simplified rotationally invariant formulation of Dudarev [19]. Atomic orbitals were used as the projector for the Hubbard U manifold [48]. The Hubbard U parameter for bulk SrVO₃ was computed using the linear response approach [49], using density functional perturbation theory (DFPT) [50]. The lattice constant for bulk SrVO₃ was fixed to the experimental value of 3.841 \AA [51] to better understand the effect of on-site Coulomb repulsion term (Hubbard U) on the t_{2g} bandwidth of bulk SrVO₃.

III. ELECTRONIC, MAGNETIC, AND STRUCTURAL PROPERTIES OF (SrRuO₃)₁/(SrTiO₃)₁(001) SL

The relationship between the structural symmetry and electronic properties in (SXO)₁/(STO)₁(001) SLs, X being a transition metal cation, has already been addressed in previous studies [14–16]. To understand the mechanism behind the MIT in (SVO)₁/(STO)₁(001) SLs, it is important to determine the correct ground state structural symmetry, at a given in-plane lattice constant. To develop a general recipe, we first study SrRuO₃ (SRO), as there are several experimental reports on electronic, magnetic, and structural aspects of both SRO bulk and ultrathin (SRO)/(STO)(001) SLs [54–60]. Moreover, SRO is a suitable choice to disentangle the effect of the Hubbard U parameter within DFT + U from the structural symmetry of such 1/1 SLs, due to the presence of weak correlation [61]. The Hubbard U term is applied to the Ru $4d$ states in this section, unless otherwise specified.

We begin by identifying the appropriate exchange-correlation functional within the KS-DFT [18] to minimize the self-interaction error. In KS-DFT, self-interaction error arises due to the spurious interaction of electrons with themselves. Self-interaction errors are small for systems with delocalized electrons but can be significant in systems with localized electrons. One way is to employ the DFT + U approach where KS-DFT is corrected by an on-site potential that removes part of the self-interaction error and hence creates the distinction between the occupied and unoccupied states, occasionally resulting in a Mott gap [62–70]. However, it remains an open question whether the Hubbard U term is addressing the self-interaction error or strong correlations? For instance, Rondinelli *et al.* [54] found that LSDA with $U = 1 \text{ eV}$ for Ru $4d$ corrects the self-interaction error in bulk SRO. An alternative approach would be to adopt an exchange-correlation functional which itself minimizes the self-interaction error, without having to include the Hubbard U parameter. The strongly constrained and appropriately normed (SCAN) meta-GGA exchange-correlation functional includes the positive orbital kinetic energy densities in addition to the electron density and its gradient in GGA [28]. It is the only semi-local exchange-correlation functional which satisfies the 17 exact constraints and is appropriately normed, i.e., it accurately calculates interactions in rare-gas atoms and unbounded systems, but also shows a promising performance for a variety of materials including Van der Waals-bonded systems as well as oxides. [71] Moreover, it is known to minimize the self-interaction error [72,73], performing especially well in correlated materials [74,75]. To show the minimization of the self-interaction error, we compare the electronic, magnetic, and structural properties of bulk SRO, obtained from PBEsol, PBEsol + U , $U = 1 \text{ eV}$, and SCAN, respectively.

Bulk SRO crystallizes in the orthorhombic ($Pbnm$) structure and is ferromagnetic for $T < 160 \text{ K}$ [52,53]. The orthorhombic structure of bulk SRO is shown in Fig. 1(a). Assuming the ideal ionic limit, a spin-only magnetic moment of $2\mu_B$ is expected, corresponding to an intermediate spin state of Ru⁴⁺ ion (d^4 , t_{2g}^3 , t_{2g}^1). The calculated lattice parameters, corresponding magnetic moments, and other structural details, listed in Table I, are in good agreement with experiment. However, the RuO₆ octahedral rotations are overestimated by PBEsol and PBEsol + U , compared to the SCAN functional, the latter reaching closest to the experimental value (see Table I).

As shown in the density of states (DOS) in Fig. 1(a), a half-metallic behavior is predicted for bulk SRO using the SCAN functional with a band gap of 1.05 eV emerging in the spin-up channel, whereas, Ru $4d$ states admixed with O $2p$ states cross the Fermi level in the spin-down channel. The valence band in the spin-up channel is formed mainly by the half-filled t_{2g}^3 orbitals up to -3 eV , below the Fermi level (see Section V of Ref. [76]), whereas the O $2p$ states predominantly contribute between -2 to -5 eV , with almost equal contribution from Ru $4d$ and O $2p$ states below -5 eV , respectively. On the other hand, in the spin-down channel, three degenerate t_{2g} orbitals, hosting a single electron, cross the Fermi energy, with O $2p$ states present mainly below -2 eV . Due to the large spatial extent of the Ru $4d$ orbitals and their hybridization with O $2p$ states, we obtain a reduced magnetic moment of $1.4\mu_B$ /Ru

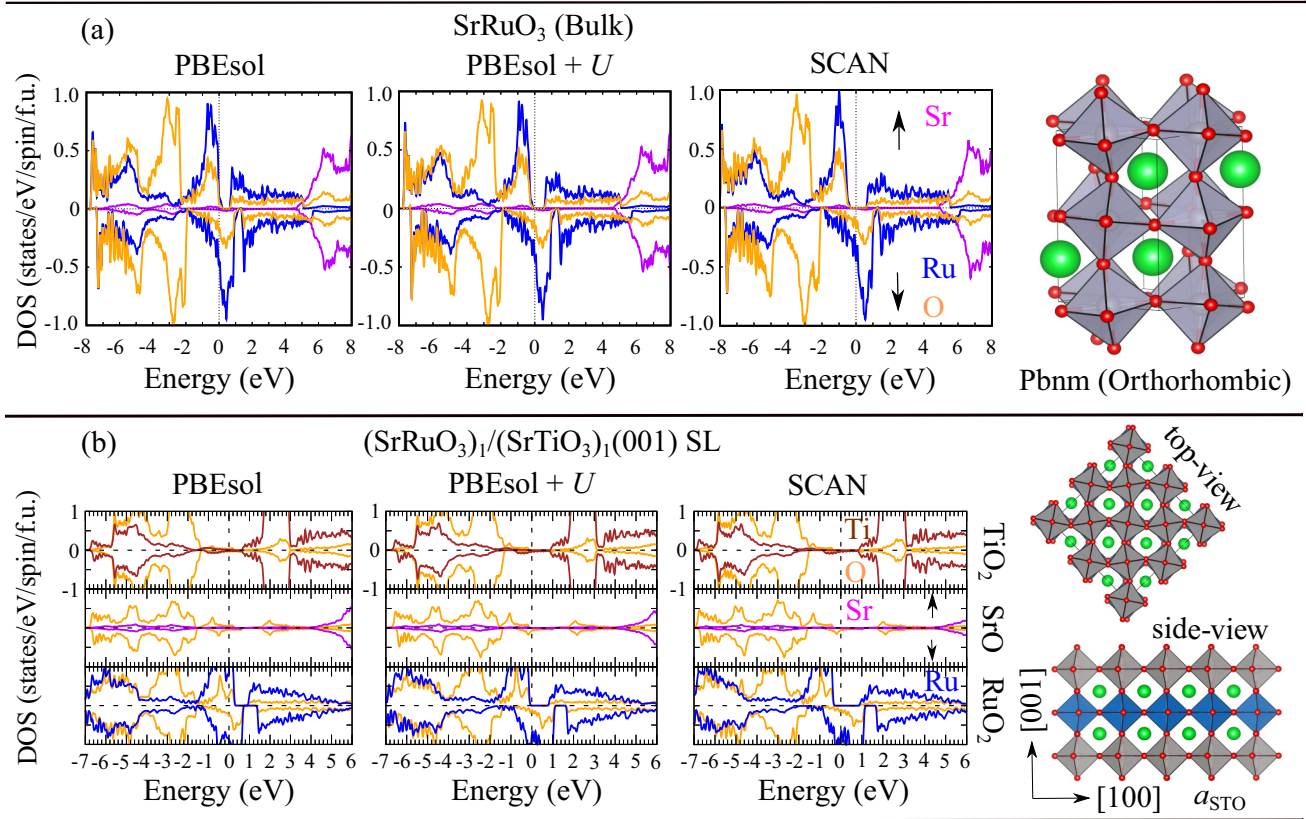


FIG. 1. (a) Projected densities of states of orthorhombic bulk SrRuO_3 ($Pbnm$ symmetry), obtained from PBEsol, PBEsol + $U = 1$ eV, and SCAN, respectively, along with the optimized crystal structure, obtained from the SCAN exchange-correlation functional. (b) Layer-, element-, and spin-resolved densities of states of tetragonal $(\text{SrRuO}_3)_1/(\text{SrTiO}_3)_1(001)$ SLs ($P4/mbm$ symmetry), obtained from PBEsol, PBEsol + U ($U = 1$ eV at Ru $4d$ and 2 eV at Ti $3d$), and SCAN, respectively, along with the top and side views of the optimized SL structure, obtained from the SCAN exchange-correlation functional. In case of SLs, the PDOS have been averaged over all corresponding sites in a supercell and normalized to one SL formula unit. In the projected density of states, blue, magenta, orange and brown color represent V, Sr, O, and Ti states, respectively. The dashed line at the zero energy represents the Fermi level.

site along with substantial magnetic moments ranging from $0.16\mu_B$ to $0.185\mu_B$ at the O sites, in contrast to the expected magnetic moment of $2\mu_B/\text{Ru}$ in the ionic limit. With the PBEsol functional the valence band maximum in the majority spin direction touches the Fermi level leading to a metallic phase. It results in a slightly reduced magnetic moment of $1.3\mu_B/\text{Ru}$ site along with magnetic moments ranging from $0.14\mu_B$ to $0.17\mu_B$ at the O sites. This indicates an overestimated delocalization of Ru $4d$ electrons with the PBEsol

functional. On the other hand, with PBEsol + U , $U = 1$ eV, the overall electronic picture of half-metallicity along with the slightly higher magnetic moment of $1.4\mu_B/\text{Ru}$ site and magnetic moments ranging from $0.14\mu_B$ to $0.17\mu_B$ at O sites, were obtained. Hence we demonstrate that for SrRuO_3 the SCAN functional minimizes the self-interaction error without having to include the Hubbard U term. Furthermore, while SCAN + U , $U = 1$ eV has a small effect on the lattice parameters and Ru magnetic moment, increasing U to 2 eV

TABLE I. Lattice parameters and the corresponding magnetic moments of the bulk SrRuO_3 obtained using PBEsol, PBEsol+ U , SCAN, and SCAN + U exchange-correlation functionals, respectively. θ is the rotation angle of RuO_6 octahedra around c axis. ϕ is tilting angle of RuO_6 octahedra. * The spread in the magnetic moment is due to the large magnetocrystalline anisotropy in SRO, and difficulty in making large single-domain samples [53]. † Two different magnetic moments at distinct Ru sites.

Exchange-correlation functional	a (Å)	b (Å)	c (Å)	θ	ϕ	μ_B
Exp. [52]	5.567	5.53	7.845	5.8	8.6	0.9–1.6*
PBEsol	5.556	5.54	7.85	7.7	9.82	1.3
PBEsol + $U = 1$ eV	5.561	5.538	7.858	7.42	9.9	1.4
SCAN	5.569	5.53	7.876	6.7	8.5	1.4
SCAN + $U = 1$ eV	5.578	5.543	7.85	6.42	8.52	1.41
SCAN + $U = 2$ eV	5.57	5.55	7.89	6.8	9.1	1.42/1.48†

TABLE II. Stabilization energy [total energy difference $\Delta E = E(P4/mmm) - E(P4/mbm)$ and $P2_1/c$] per supercell] of the $(\text{SrRuO}_3)_1/(\text{SrTiO}_3)_1(001)\text{SL}$ at a_{STO} .

Exchange-correlation functional	ΔE ($P4/mbm$) (in meV)	ΔE ($P2_1/c$) (in meV)
PBEsol	784	744
SCAN	840	816
PBEsol + U ($U_{\text{Ru}} = 1$ eV, $U_{\text{Ti}} = 2$ eV)	1248	1200
PBEsol + U ($U_{\text{Ru}} = 3$ eV, $U_{\text{Ti}} = 2$ eV)	1152	1216
SCAN + U ($U_{\text{Ru}} = 2$ eV)	760	1128

increases slightly the RuO_6 rotation, tilt angles, and the magnetic moments (see Table I).

We now turn to discuss the electronic, magnetic, and structural properties of the SRO monolayer confined between the STO spacer layers in a $1/1(001)$ -oriented SL, displayed in Fig. 1(b). The in-plane lattice constant was fixed to the experimental lattice constant of bulk STO ($a = 3.905 \text{ \AA}$), modeling epitaxial growth on $\text{STO}(001)$ substrate, thus the SRO monolayer is under compressive strain (-0.46%). To assess the role of the exchange-correlation functional, we again performed calculations using PBEsol, PBEsol + U , $U = 1$ eV, and SCAN. In bulk STO, similar band gaps of 2.17 and 2.21 eV, were obtained using PBEsol + U , $U = 2$ eV at Ti 3d and SCAN, respectively (see section IV of the supplement [76]). Therefore $U = 2$ eV at Ti 3d was employed in all the PBEsol + U calculations for $(\text{SRO})_1/(\text{STO})_1(001)$ SL. The effect of different exchange-correlation functionals on the lattice parameters and the band gap of bulk STO are provided in Table VI (Sec. IV) of the supplement [76]. The structural parameters, especially the TiO_6 octahedral rotations, are best described by the SCAN functional, in agreement with the recent work on bulk STO [77]. Notably, with SCAN + U , $U = 2$ eV, the TiO_6 octahedral rotations were found to be severely overestimated, compared to experiment.

Importantly, the SRO monolayer is known to adopt the low temperature tetragonal ($I4/mcm$) phase of STO, having antiferrodistortive (AFD) rotations ($a^0a^0c^-$) of the neighboring TiO_6 octahedra, resulting in overall tetragonal ($P4/mbm$) symmetry in the $1/1$ SL [see Fig. 1(b)] [55–58,60]. With this we proceed to determine the ground state structural symmetry of $(\text{SRO})_1/(\text{STO})_1(001)$ SL.

To account for possible symmetry reductions beyond the tetragonal ($P4/mmm$) symmetry, we allowed in-plane octahedral rotations around the $[001]$ axis, and subsequently both octahedral rotations and tilts, resulting in tetragonal ($P4/mbm$) and monoclinic ($P2_1/c$) symmetries, respectively. The total energy difference between the tetragonal ($P4/mmm$) symmetry and the other two symmetries, obtained using the different exchange-correlation functionals are displayed in Table II. SCAN, PBEsol and PBEsol + U , $U = 1$ eV correctly render the tetragonal ($P4/mbm$) symmetry of the $1/1$ SL. To determine the effect of Hubbard U term on the structural sym-

metry, additional calculations using SCAN + U ($U = 2$ eV) and PBEsol + U ($U = 3$ eV) were performed. This results in a monoclinic ($P2_1/c$) symmetry. Thus we conclude that the Hubbard U term, beyond a critical value which depends on the exchange-correlation functional, favors the monoclinic ($P2_1/c$) symmetry in $(\text{SRO})_1/(\text{STO})_1(001)$ SL.

Adopting the correct tetragonal ($P4/mbm$) symmetry for $(\text{SRO})_1/(\text{STO})_1(001)$ SL and constraining to the lattice parameter of the STO substrate ($a = 3.905 \text{ \AA}$), the optimized cross-plane lattice constants are $c = 3.94 \text{ \AA}$ (PBEsol), 3.95 \AA (PBEsol + U , $U = 1$ eV), 3.96 \AA (PBEsol + U , $U = 3$ eV), 3.95 \AA (SCAN), and 3.96 \AA (SCAN + U , $U = 2$ eV). To show the correction of self-interaction error, we compare the electronic and magnetic properties obtained from PBEsol, PBEsol + U , $U = 1$ eV, and SCAN which result in the correct ground state with tetragonal ($P4/mbm$) symmetry. Detailed structural parameters for the above three cases are provided in Table I (Sec. I) of Ref. [76].

From the TiO_2 panels of the projected density of states, shown in Fig. 1(b), we infer that the Fermi energy is located in the STO band gap, pinned by the Ru 4d states. Further, from the RuO_2 panels, half-metallicity due to band gap openings of 1.26 and 0.97 eV in the spin-up channel along with Ru 4d states predominantly crossing the Fermi level in the spin-down channel, are observed from SCAN and PBEsol + U , respectively. The compressive strain lifts the degeneracy of Ru 4d t_{2g} orbitals of the confined SRO layer, shifting the d_{xy} orbital lower in energy compared to degenerate d_{xz} , d_{yz} orbitals (see Sec. V of Ref. [76]) due to a Jahn-Teller distortion expressed in a slight elongation of the Ru-O apical, compared to the basal Ru-O bond lengths.

In contrast, a fully metallic phase was obtained from the PBEsol functional as the valence band maximum touches the Fermi level. This results in a highly underestimated magnetic moment at the Ru sites of $0.74\mu_B$ along with magnetic moments ranging from $0.084\mu_B$ to $0.125\mu_B$ at the O sites. In comparison, the magnetic moments of Ru and O sites obtained with PBEsol + U are $1.41\mu_B$ and $0.174\mu_B$ - $0.18\mu_B$, respectively. Similar values are obtained with SCAN: $1.41\mu_B/\text{Ru}$ sites along with O site magnetic moments of $0.195\mu_B$. Ti remained nonmagnetic in all cases. Note that the magnetic moment at the Ru site ($0.74\mu_B$) obtained with PBEsol in the $1/1$ SL is underestimated compared to bulk SRO ($1.3\mu_B/\text{Ru}$) due to d_{xz} , d_{yz} orbitals crossing the Fermi level in the former compared to only d_{yz} orbital crossing Fermi level in the latter (see Sec. V of Ref. [76]).

Overall, the SCAN exchange-correlation functional best describes the electronic, magnetic, and structural properties of $(\text{SRO})_1/(\text{STO})_1(001)$ SL, by minimizing the self-interaction error, without having to include the Hubbard U term. Upon inclusion of Hubbard $U = 2$ eV, the energy band gaps of the $1/1$ SL with tetragonal ($P4/mbm$) symmetry in the spin-up channel widened to 1.36 and 1.74 eV for PBEsol + U , $U = 3$ eV and SCAN + U , $U = 2$ eV, respectively, preserving the halfmetallic behavior. Lastly, SRO bulk, thin films, and $(\text{SRO})_1/(\text{STO})_1(001)$ SLs are known to exhibit large magneto-crystalline anisotropy energies (MAE) [53,78–83]. For completeness, we also provide a comparative analysis of MAE's in bulk SRO and $(\text{SRO})_1/(\text{STO})_1(001)$ SL in Sec. II of Ref. [76]. We find that the easy axis along the

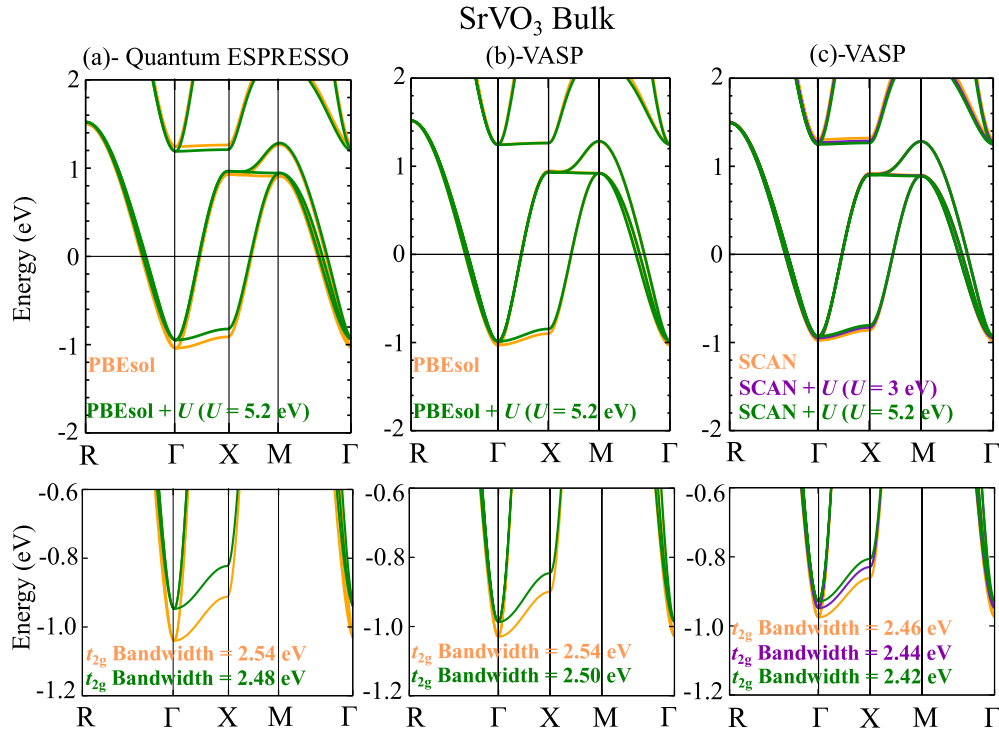


FIG. 2. Energy band structure diagrams of nonmagnetic cubic ($Pm\bar{3}m$) bulk SrVO_3 obtained from (a) QUANTUM ESPRESSO code using PBEsol (orange color bands) and PBEsol + U ($U = 5.2$ eV at V $3d$, dark-green color bands), respectively, (b) VASP code using PBEsol (orange color bands) and PBEsol + U ($U = 5.2$ eV at V $3d$, dark-green color bands), respectively, and (c) VASP code using SCAN (orange color bands) and SCAN + U ($U = 3$ eV at V $3d$, violet color bands and $U = 5.2$ eV at V $3d$, dark-green color bands), respectively (top panels). The relative shift of the bottom of t_{2g} bands from different exchange-correlation functionals in each case is shown in the band structure diagrams (bottom panels), plotted in the energy range of -1.2 to -0.6 eV.

[010] direction in bulk SRO changed to [001] direction in $(\text{SRO})_1/(\text{STO})_1(001)$ SL.

IV. ASSESSING STRONG CORRELATION IN BULK SrVO_3

Now we turn to bulk SVO (d^1) which is a paramagnetic metal at all temperatures and crystallizes in a cubic perovskite structure (space group: $Pm\bar{3}m$) with the lattice parameter of $a = 3.84$ Å [84–88]. Moreover, experimentally it is classified as a correlated metal [89–97]. Angle resolved photoemission spectra (ARPES) measurements reveal a substantial t_{2g} band narrowing by a factor of two compared to the local density approximation (LDA) bandwidth (2.6 eV) due to strong electronic correlation [95].

Employing linear response approach via density functional perturbation theory (DFPT) as implemented in the QUANTUM ESPRESSO code, a Hubbard U parameter of 5.2 eV was obtained at the V- $3d$ site. Although the value may not be directly transferable to VASP, it still provides an estimate. Figure 2(a) shows the comparison of the band structures from PBEsol and PBEsol + U ($U = 5.2$ eV) with t_{2g} bandwidths of 2.54 and 2.48 eV, respectively, obtained using the QUANTUM ESPRESSO code.

Nearly identical values for t_{2g} bandwidths are obtained with VASP: 2.54 eV (PBEsol) and 2.50 eV (PBEsol + U , $U = 5.2$ eV), as shown in Fig. 2(b). Interestingly, the PBEsol functional, irrespective of the DFT code used, resulted in the same t_{2g} bandwidth of 2.54 eV, albeit with a small upward shift

in the bottom of the t_{2g} bands in case of VASP [see Figs. 2(a) and 2(b) (bottom panels)]. The SCAN functional (VASP) itself resulted in a lower t_{2g} bandwidth of 2.46 eV [see Fig. 2(c)], compared to PBEsol + U (VASP). This clearly indicates the higher localization of electrons by the SCAN functional due to the minimization of the self-interaction error, compared to the PBEsol functional, similar to the cases of bulk SrRuO_3 and $(\text{SRO})_1/(\text{STO})_1(001)$ SL (see Sec. III above). This finding is outlined diagrammatically in Fig. 6(a). Lastly, upon inclusion of Hubbard $U = 3$ and 5.2 eV with SCAN, bandwidths were further reduced by 20 and 40 meV, respectively.

V. EFFECT OF HUBBARD U AND LATERAL LATTICE CONSTANT ON $(\text{SrVO}_3)_1/(\text{SrTiO}_3)_1(001)$ SL

We now turn to discuss the structural symmetry of the $(\text{SVO})_1/(\text{STO})_1(001)$ SL at the lateral lattice constants of bulk SrTiO_3 (a_{STO}) and YAlO_3 (a_{YAO}), respectively. Note that since the SCAN functional itself has a higher effect on V $3d$ states of bulk SVO, compared to PBEsol + U ($U = 5.2$ eV, see Sec. IV), we employ SCAN and SCAN + U ($U = 2$ and 3 eV at V $3d$ states) to systematically highlight the role of Hubbard U term on the MIT and possible symmetry breaking in $(\text{SVO})_1/(\text{STO})_1(001)$ SL, at a given lateral lattice constant. Guided by the discussions so far, we compare the relative stability of distinct structural symmetries, obtained by allowing octahedral rotations and/or tilts, in addition to the tetragonal ($P4/mmm$) symmetry in the 1/1 SL. Also, the

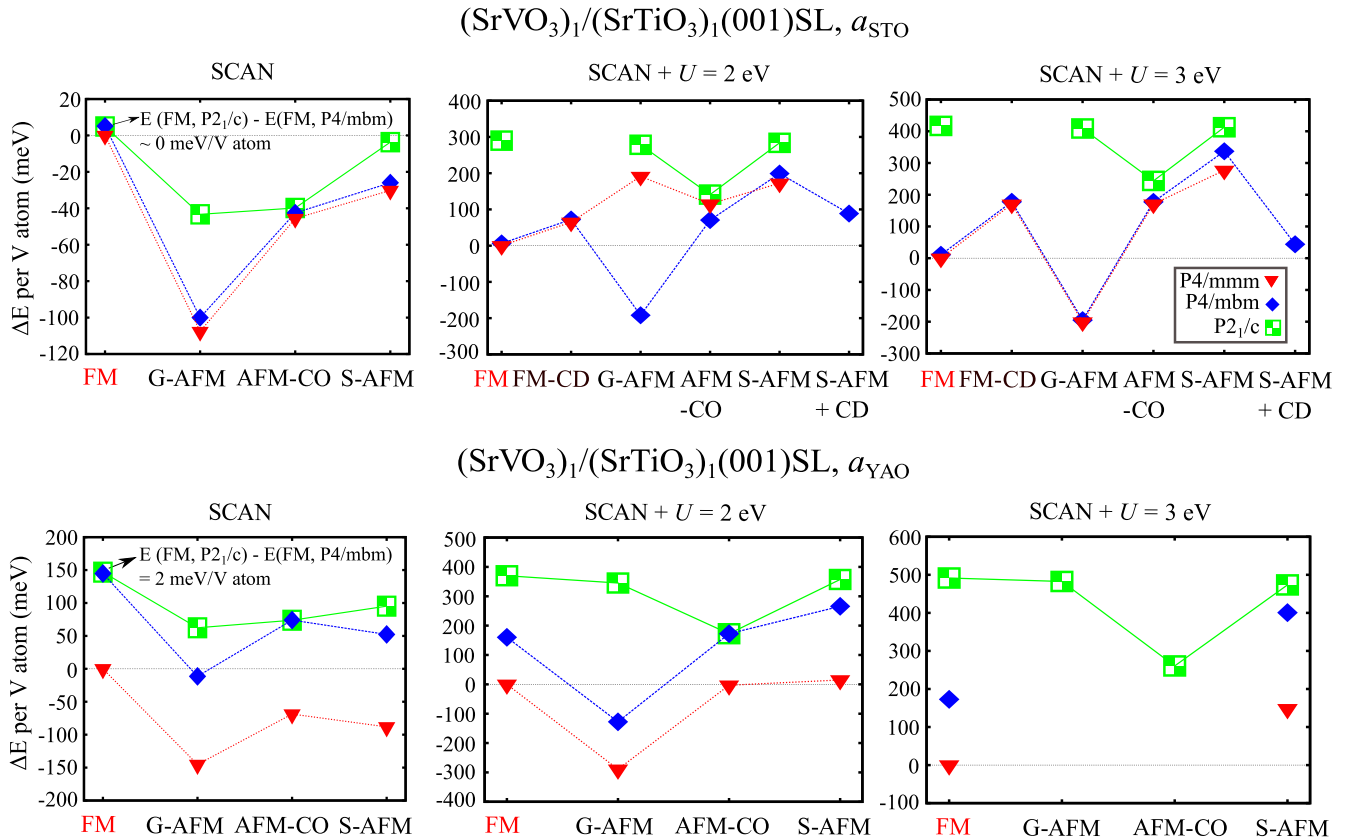


FIG. 3. The left to right panels show the results from SCAN, SCAN + $U = 2$ and 3 eV, at a_{STO} (top) and a_{YAO} (bottom), respectively. The plotted points are relative energy differences (ΔE) between different possible magnetic orders in $(\text{SrVO}_3)_1/(\text{SrTiO}_3)_1(001)$ SLs, having tetragonal ($P4/mmm$ or $P4/mbm$), and monoclinic ($P2_1/c$) symmetries each, obtained by setting the total energy of the FM order in tetragonal ($P4/mmm$) symmetry as the reference in all the panels, i.e., $\Delta E = E(\text{FM}, P4/mmm) - E(\text{magnetic order}; \text{structural symmetry})$.

relative stability of different possible magnetic configurations, at each structural symmetry, were obtained with the SCAN exchange-correlation functional, plotted in Fig. 3. We remind that the tetragonal ($P4/mmm$) symmetry is the highest possible symmetry by construction in $(\text{SXO})_1/(\text{STO})_1(001)$ SLs, X being the transition metal cation. We have considered the following cases: ferromagnetic (FM), ferromagnetic charge disproportionated (FM-CD), antiferromagnetic G-type ordered (G-AFM); antiferromagnetic with charge-ordering (AFM-CO) [98]; antiferromagnetic with stripe order (S-AFM) [see Fig. 6(b)]; and antiferromagnetic with stripe order and charge disproportionation (S-AFM + CD), respectively.

Using the SCAN functional FM order was found to be most stable, irrespective of in-plane lattice constant and structural symmetry, shown in Fig. 3. The relative stability of different structural symmetries and magnetic order are calculated with respect to the FM case with tetragonal symmetry, i.e., $\Delta E = E(\text{FM}, P4/mmm) - E(\text{magnetic order}; \text{structural symmetry})$. At a_{STO} , we find that the tetragonal ($P4/mbm$) and monoclinic ($P2_1/c$) symmetries are nearly energetically degenerate, and more favorable than the tetragonal ($P4/mmm$) symmetry by 5 meV per V atom. In contrast, at a_{YAO} , the monoclinic ($P2_1/c$) symmetry is distinctly more stable than the tetragonal ($P4/mbm$) symmetry by 2 meV per V atom, and the tetragonal ($P4/mmm$) symmetry by 147 meV per V atom, respectively. This clearly indicates that the energy gain in monoclinic ($P2_1/c$) symmetry is contributed mainly by the

in-plane XO_6 , $X = \text{V}$, or Ti , octahedral rotations about the $[001]$ axis, rather than their tilts. This is further confirmed by the structural details obtained from the SCAN functional (see Sec. I of Ref. [76]). In summary, the FM metallic character due to occupation of the degenerate t_{2g} orbitals at the V sites was obtained with the SCAN functional, irrespective of the in-plane lattice constant and structural symmetry (discussed further below in Secs. VI and VII).

Upon including a Hubbard U term, at a_{STO} , we obtain monoclinic ($P2_1/c$) symmetry as the ground state (see Fig. 3), along with the opening of a band gap of 0.6 eV ($U = 2$ eV) and 1.05 eV ($U = 3$ eV), respectively (see Sec. III of Ref. [76]). In agreement with the previous reports [14–16], in monoclinic ($P2_1/c$) symmetry, an orbital reconstruction occurs with an alternating occupation of d_{xz}/d_{yz} orbitals at neighboring V sites (orbital-ordering) along with FM spin alignment. This is at variance with the recent finding of d_{xy} orbital occupation at the V sites in SVO ultrathin film, deposited on a STO(001) substrate [23,25]. Moreover, neither of the bulk components has octahedral tilts. Hence, corroborating the findings of Section III, we conclude that SCAN + U always favors the monoclinic ($P2_1/c$) symmetry i.e. spatial-symmetry breaking, irrespective of in-plane lattice constant. This also confirms that the SCAN functional is sufficient to determine the structural symmetry of $(\text{SXO})_1/(\text{STO})_1(001)$ SLs, $X = \text{V}$, Ru, at a given in-plane lattice constant.

Based on the findings so far we outline a recipe: (1) Ground state structural symmetry. Apart from minimizing the self-interaction error in TMOs, the SCAN functional correctly predicts the ground state structural symmetry of $(\text{SXO})_1/(\text{STO})_1(001)$ SLs, X being the transition metal cation, at a given in-plane lattice constant, by allowing symmetry reductions. However, we argue that the electronic properties might be inaccurately described by the SCAN functional if an additional Hubbard U is needed to lift the t_{2g} or e_g orbital degeneracy, and open a Mott-Hubbard type band gap, as e.g., in the $(\text{SVO})_1/(\text{STO})_1(001)$ SL (discussed in Secs. VI–VIII below). Also, spin-orbit coupling (SOC) might be important in $X = 4d$ and $5d$ transition metal cations, e.g., in the $(\text{SRO})_1/(\text{STO})_1(001)$ SL (discussed in Sec. II of Ref. [76]).

(2) Artificial symmetry breaking by Hubbard U . SCAN + U favors the monoclinic ($P2_1/c$) symmetry in $(\text{SXO})_1/(\text{STO})_1(001)$ SLs, X being the transition metal cation, irrespective of in-plane lattice constant and X . Hence SCAN + U might not be suitable to determine the ground state structural symmetry.

(3) Static correlations. To include the static correlation in $(\text{SXO})_1/(\text{STO})_1(001)$ SLs, X being the transition metal cation, a Hubbard U term in combination with the SCAN functional can be employed by adopting the correct structural symmetry, obtained from the SCAN functional. Note that effects like CD or orbital polarization can lead to further symmetry lowering.

VI. ELECTRONIC AND MAGNETIC PROPERTIES OF $(\text{SrVO}_3)_1/(\text{SrTiO}_3)_1(001)$ SL AT a_{STO}

Following the above recipe, we now discuss the effect of including static correlation in $(\text{SVO})_1/(\text{STO})_1(001)$ SL by adopting the tetragonal ($P4/mbm$) symmetry obtained from the SCAN functional, at a_{STO} (see Fig. 3). When constrained to the lattice parameter of the STO substrate ($a = 3.905 \text{ \AA}$), the optimized cross-plane lattice constants are $c = 3.875 \text{ \AA}$ (FM), 3.895 \AA (S-AFM), and 3.9 \AA (S-AFM), obtained from SCAN, SCAN + $U = 2$ and 3 eV , respectively. Figure 4 shows the optimized geometry of the $(\text{SVO})_1/(\text{STO})_1(001)$ SL, obtained from SCAN. Further structural details are provided in Section I of Ref. [76], whereas the relative stability of different possible magnetic orders are plotted in Fig. 3.

The FM metallic phase results from the d^1 occupation of the degenerate t_{2g} orbitals at the V site (magnetic moment of $0.97 \mu_B$, see Figs. 4 and 5). Upon including $U = 2$ and 3 eV , the degeneracy of t_{2g} orbitals is subsequently lifted. This goes hand in hand with a vertical compression of VO_6 octahedra under tensile strain (Jahn-Teller distortion), resulting in a uniform occupation of the d_{xy} orbital at the V sites [see integrated spin density plot in Fig. 4(b)], leaving the d_{xz} , d_{yz} orbitals empty (see Sec. V of Ref. [76]). Simultaneously, a long-range S-type AFM order [Fig. 6(b)] is stabilized by 192 meV per V site ($U = 2 \text{ eV}$) and 326 meV per V site ($U = 3 \text{ eV}$), respectively, compared to the FM order. Notably, the S-type AFM order is further accompanied by a symmetry-breaking from the tetragonal ($P4/mbm$) to orthorhombic ($Cmmm$) symmetry, characterized by distinct

V-O-V bond angles along the $[110]$ (173.71° and 173.28° at $U = 2$ and 3 eV , respectively) and $[\bar{1}10]$ (175.93° and 175.73° at $U = 2$ and 3 eV , respectively) axes.

The orbital polarization results in a correlation and confinement driven Mott-type band gap openings of 0.2 eV ($U = 2 \text{ eV}$) and 0.73 eV ($U = 3 \text{ eV}$), respectively (see Figs. 4 and 5). Notably, the present Mott-insulating phase is different from the FM metallic orbital-ordered state with uniform V $3d_{xy}$ orbital occupation that turns insulating in the presence of spin-orbit coupling, obtained by Pardo and Pickett [9]. Also, similar Mott insulating phase with G-type AFM order was reported previously in LaTiO_3 (Ti, d^1) Mott insulator when confined in $(\text{LaTiO}_3)_n/(\text{LaAlO}_3)_5(001)$ multilayer systems with $n = 1-3$ [99].

Concerning the band alignments, from the layer-resolved density of states (Fig. 4), we infer that the V $3d$ states lie in the STO band gap. In contrast to the FM phase where the V $3d$ states cross the Fermi level, E_F lies either at the top of the valence band ($U = 2 \text{ eV}$), or in the STO band gap ($U = 3 \text{ eV}$) for the AFM stripe phase.

At $U = 3 \text{ eV}$, a significantly higher V $3d$ -O $2p$ hybridization in the vicinity of the VBM [between -1 eV and E_F] along with a reduced valence bandwidth were inferred from the layer-resolved density of states, compared to $U = 2 \text{ eV}$ [Fig. 4(b)]. Moreover, the in-plane $3d_{xy}$ orbital occupation results in dispersionless flat bands along the vertical direction Γ -Z (see Fig. 5). We further point out that the S-type AFM order must not be interpreted as the perfect 2D spin order in our case due to the presence of finite interlayer coupling between the SVO sublayers in SVO/STO SLs [8], hence not conflicting with Mermin and Wagner's theorem [100]. Moreover, similar quasi-2D AFM order has been previously reported in other $S = 1/2$, V based compounds, for instance in CaV_4O_9 [101] and $\text{Zn}_2\text{VO}(\text{PO}_4)_2$ [102]. Finally, we point out that although $U = 2 \text{ eV}$ is sufficient to open the quasi Mott-Hubbard type band gap, an energetically more favorable S-type AFM order is obtained at $U = 3 \text{ eV}$ (see Fig. 3). This indicates the presence of long-range magnetic order in $(\text{SVO})_1/(\text{STO})_1(001)$ SL, different from the Néel type (G-AFM) Mott-insulating phase in SrO terminated SVO ultrathin film on a STO(001) substrate [23].

Previously, a CD ($V^{4+} \rightarrow V^{4+\delta} + V^{4-\delta}$) solution was obtained with tetragonal ($P4/mmm$) symmetry [14]. However, by using the laterally enlarged ($2\sqrt{2}a \times 2\sqrt{2}a$) $R45^\circ$ SL, we obtain FM-CD to be less stable than the S-type AFM order (Fig. 3). We mention here analogies to the CD leading to MIT in ($S = 1/2$) rare earth nickelates, e.g., YNiO_3 or LuNiO_3 [24]. The FM-CD in the tetragonal ($P4/mbm$) symmetry is accompanied by a breathing mode distortion of the VO_6 octahedra (octahedral volumes: $9.18/10.8 \text{ \AA}^3$ ($U = 2 \text{ eV}$) and $9.09/10.96 \text{ \AA}^3$ ($U = 3 \text{ eV}$) at the two V sites, respectively and further reflected in the distinct magnetic moments of $0.25/1.68 \mu_B$ ($U = 2 \text{ eV}$) and $0.14/1.79 \mu_B$ ($U = 3 \text{ eV}$), respectively, at the alternating V sites. The breathing mode leads to a further symmetry-breaking from the tetragonal ($P4/mbm$) to tetragonal ($P4/m$) symmetry.

At $U = 2 \text{ eV}$, the Fermi level separates the degenerate occupied $3d_{xz}/d_{yz}$ states from the unoccupied $3d_{xy}$ state, rendering the system at the verge of a MIT. While here the unoccupied and occupied parts are touching, at $U = 3 \text{ eV}$ they

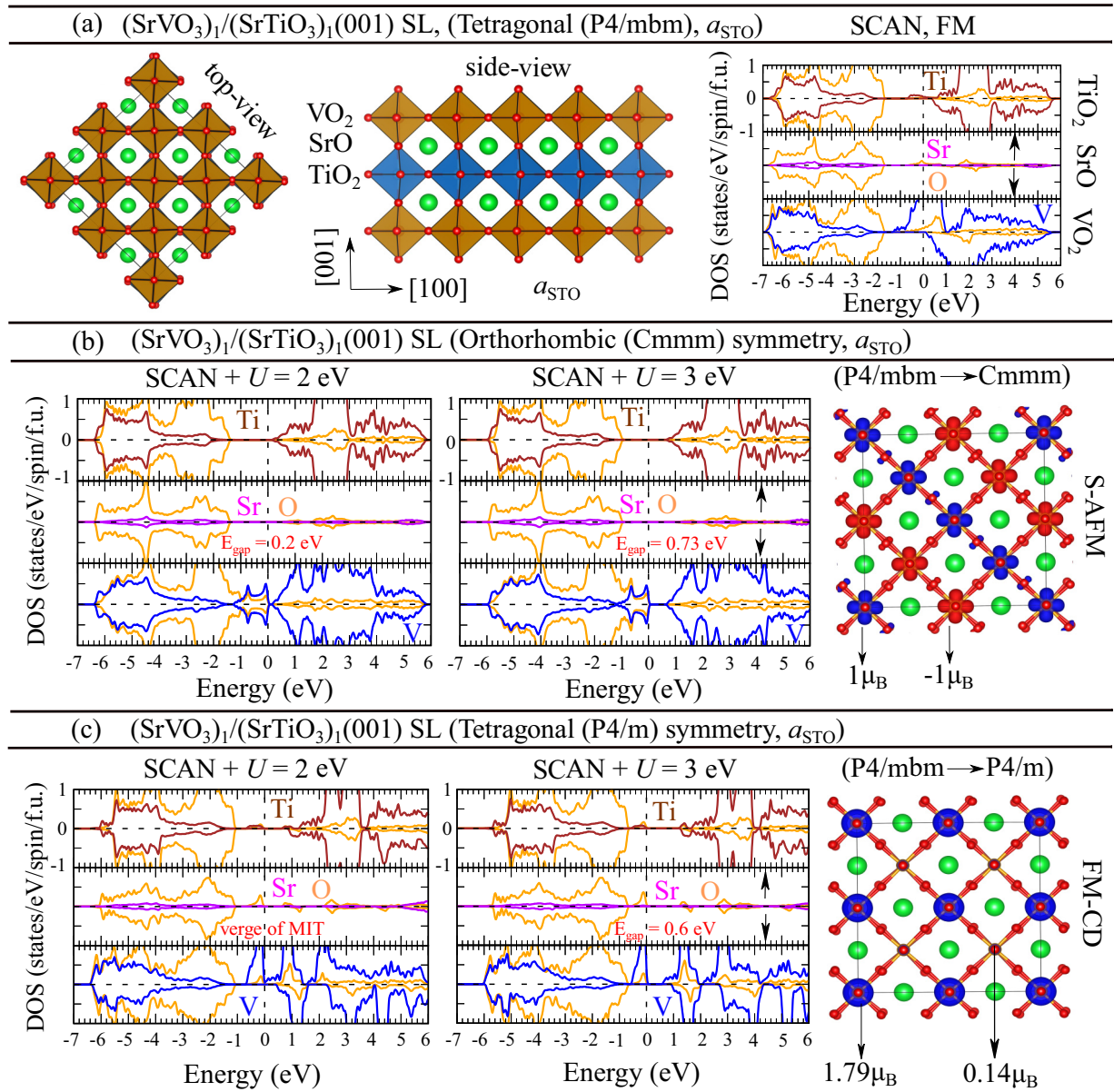


FIG. 4. (a) Top and side views of the optimized tetragonal $(\text{SrVO}_3)_1/(\text{SrTiO}_3)_1(001)$ SL ($P4/mbm$ symmetry) at a_{STO} , along with layer-, element-, and spin-resolved densities of states, obtained from SCAN functional. (b) Layer-, element-, and spin-resolved densities of states of orthorhombic $(\text{SrVO}_3)_1/(\text{SrTiO}_3)_1(001)$ SL ($Cmmm$ symmetry) at a_{STO} , from SCAN + $U = 2$ and 3 eV, respectively, and the corresponding integrated spin density plot (integrated from -7 eV to the Fermi level (0 eV)) at $U = 3$ eV; further displays the S-type AFM order and site wise spin magnetic moments, respectively. (c) Layer-, element-, and spin-resolved densities of states of tetragonal $(\text{SrVO}_3)_1/(\text{SrTiO}_3)_1(001)$ SL ($P4/m$ symmetry) at a_{STO} , obtained from SCAN + $U = 2$ and 3 eV, respectively, and the corresponding integrated spin density plot [integrated from -7 eV to the Fermi level (0 eV)] at $U = 3$ eV; further displays the FM charge-disproportionation and site wise spin magnetic moments, respectively. In case of SLs, the PDOS have been averaged over all corresponding sites in a supercell and normalized to one SL formula unit. Blue and red colors in the integrated spin density plots represent the spin-up and spin-down channels, respectively. In the projected densities of states, blue, magenta, orange and brown color represent V, Sr, O, and Ti states, respectively. The dashed line at the zero energy represents the Fermi level.

are separated leading to a band gap of 0.6 eV and an enhanced CD, as shown in the spin density plot [see Fig. 4(c)].

VII. MOTT-HUBBARD TRANSITION IN $(\text{SrVO}_3)_1/(\text{SrTiO}_3)_1(001)$ SL AT a_{STO}

To ascertain the Mott-Hubbard type MIT in the $(\text{SVO})_1/(\text{STO})_1(001)$ SL at a_{STO} , without including any structural distortions (octahedral rotations and/or tilts) that

lower the symmetry, we now adopt the tetragonal ($P4/mmm$) symmetry, albeit 5 meV per V atom less stable than the tetragonal ($P4/mbm$) symmetry (see Fig. 3). Such an MIT, stemming solely from the strong electronic correlation is outlined diagrammatically in Fig. 6(a).

When constrained to the lateral lattice constant of bulk STO ($a = 3.905 \text{ \AA}$), the optimized cross-plane lattice constants are 3.89 \AA (FM), 3.85 \AA (G-AFM), and 3.89 \AA (S-AFM), obtained using SCAN, SCAN + U , $U = 2$ and 3 eV,

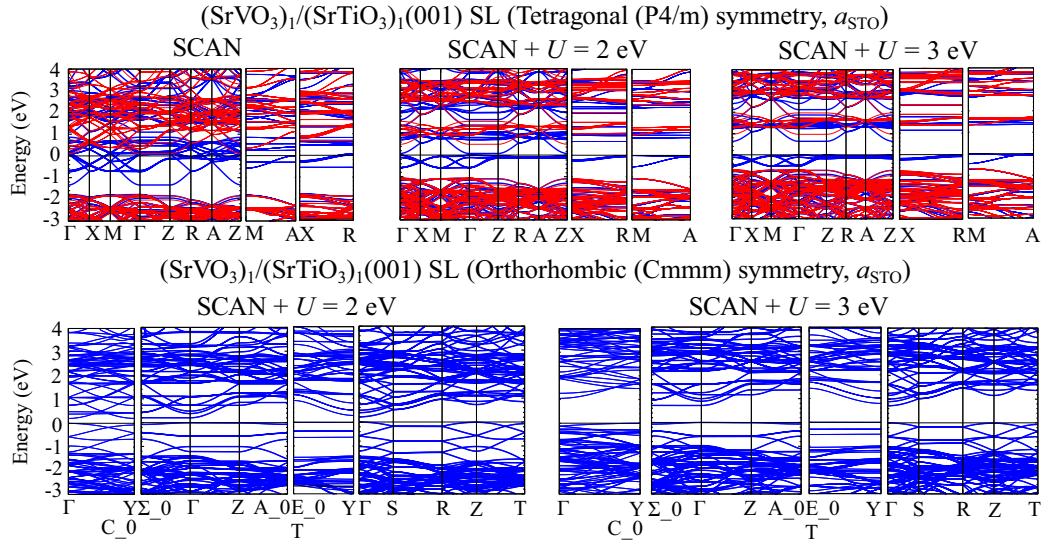


FIG. 5. (Top) Band structure diagrams of the tetragonal $(\text{SrVO}_3)_1/(\text{SrTiO}_3)_1(001)$ SL at a_{STO} , obtained from SCAN ($P4/mmm$ symmetry), and SCAN + $U = 2$ and 3 eV ($P4/m$ symmetry), respectively. (Bottom) Band structure diagrams of the orthorhombic $(\text{SrVO}_3)_1/(\text{SrTiO}_3)_1(001)$ SL ($Cmmm$ symmetry) at a_{STO} , obtained from SCAN + $U = 2$ and 3 eV, respectively. Blue and red bands correspond to spin-up and spin-down channels, respectively.

respectively. Further structural details are provided in Sec. I of Ref. [76]. Figure 6(c) shows the optimized structure of the 1/1 SL, obtained with SCAN. Similar to the findings of Sec. VI, we obtain a long-range S-type AFM order, with FM and AFM coupling of V spins along the $[\bar{1}10]$ and $[110]$ directions, respectively [see Fig. 6(b)], from SCAN + U , $U = 3$ eV. On the other hand, the ground state is FM with SCAN and G-type AFM with $U = 2$ eV. Note that the $3d_{xy}$ orbital is uniformly occupied at all the V sites due to the out-of-plane compression of the VO_6 octahedra under tensile strain at both U values, shown in the spin density plots in Fig. 6(c). In contrast to the metallic FM phase, obtained with SCAN, Mott-type band gaps of 0.54 eV ($U = 2$ eV) and 0.70 eV ($U = 3$ eV) were obtained, respectively [see Fig. 6(c)] and a magnetic moment of $1 \mu_B/\text{V}$ site. From the VO_2 panels of the projected density of states, we observe a significantly higher V $3d$ -O $2p$ hybridization in the vicinity of the VBM (between -1 eV up to E_F) at $U = 3$ eV, compared to $U = 2$ eV.

Lastly, we wish to point out that the tetragonal ($P4/mmm$) symmetry was preserved throughout the MIT, hence proving the dominant role of strong electronic correlation behind the Mott-type MIT in $(\text{SVO})_1/(\text{STO})_1(001)$ SL at a_{STO} . Furthermore, the persistence of a Mott insulating phase of the energetically favored S-type AFM order at $U = 3$ eV, in both the tetragonal ($P4/mmm$) and orthorhombic ($Cmmm$) symmetry is in agreement with a similar finding in SrO terminated SVO ultrathin film on $\text{STO}(001)$ substrate [23].

VIII. ELECTRONIC AND MAGNETIC PROPERTIES OF $(\text{SrVO}_3)_1/(\text{SrTiO}_3)_1(001)$ SL AT a_{YAO}

Engineering desired electronic and magnetic phases using large epitaxial strain (up to 8% (uniaxial) and 5% (biaxial)) has been recently reported in the nanoscale $\text{La}_{0.7}\text{Ca}_{0.3}\text{MnO}_3$ oxide membranes [103]. In this section, we discuss the effect of including strong correlations in $(\text{SVO})_1/(\text{STO})_1(001)$ SL

by adopting the monoclinic ($P2_1/c$) symmetry, obtained from the SCAN functional at a_{YAO} . When constrained to the lattice constant of bulk YAO substrate ($a_{pc} = 3.708 \text{ \AA}$), the optimized cross-plane lattice constants $c = 4.04, 4.07,$ and 4.08 \AA are obtained using SCAN, SCAN + $U = 2$ and 3 eV, respectively. Further structural details are provided in Sec. I of Ref. [76], whereas the relative stability of different possible magnetic orders are plotted in Fig. 3.

With the SCAN functional, the FM metallic phase results from the degenerate $3d_{xz}/d_{yz}$ states, predominantly crossing the Fermi energy, whereas, the $3d_{xy}$ state is pushed up and crosses the Fermi level with concomitant out-of-plane elongation of the VO_6 octahedra, under compressive strain (see Secs. I and V of Ref. [76]). Structural distortions in the monoclinic ($P2_1/c$) symmetry, obtained from the SCAN functional, comprise VO_6 (TiO_6) octahedral rotations around the $[001]$ axis, as reflected by the V-O-V (Ti-O-Ti) angle of $174.9^\circ(156.5^\circ)$, compared to the negligible octahedral tilts (V-O-Ti angle of $\sim 180^\circ$).

Upon including a Hubbard U parameter, the V-O-V bond angles reduce to 165.2° and 164° at $U = 2$ and 3 eV, respectively, while leaving the Ti-O-Ti angles qualitatively unchanged. Interestingly, we obtain a very slight reduction in the V-O-Ti bond angles, i.e., 178.9° and 179.5° at $U = 2$ and 3 eV, respectively. Next, finite octahedral rotations accompanied by the distinct V-O bond lengths of 1.93 \AA and 1.81 \AA along $[110]$ and $[\bar{1}10]$ directions at $U = 2$ eV, respectively, and tilts drive the orbital reconstruction, using the larger $2\sqrt{2}a \times 2\sqrt{2}a \times 2c$ SL, leading to an alternating occupation of $3d_{xz}/d_{yz}$ orbitals at the neighboring V sites (orbital order), along with FM spin alignment, as shown in the spin density plot (Fig. 7). FM orbital ordering, in turn leads to a band gap opening of 0.6 eV ($U = 2$ eV) and 1.15 eV ($U = 3$ eV), respectively. It is noteworthy that the FM orbital order was stabilized by the Hubbard U parameter, outlining its key role along with confinement to induce a

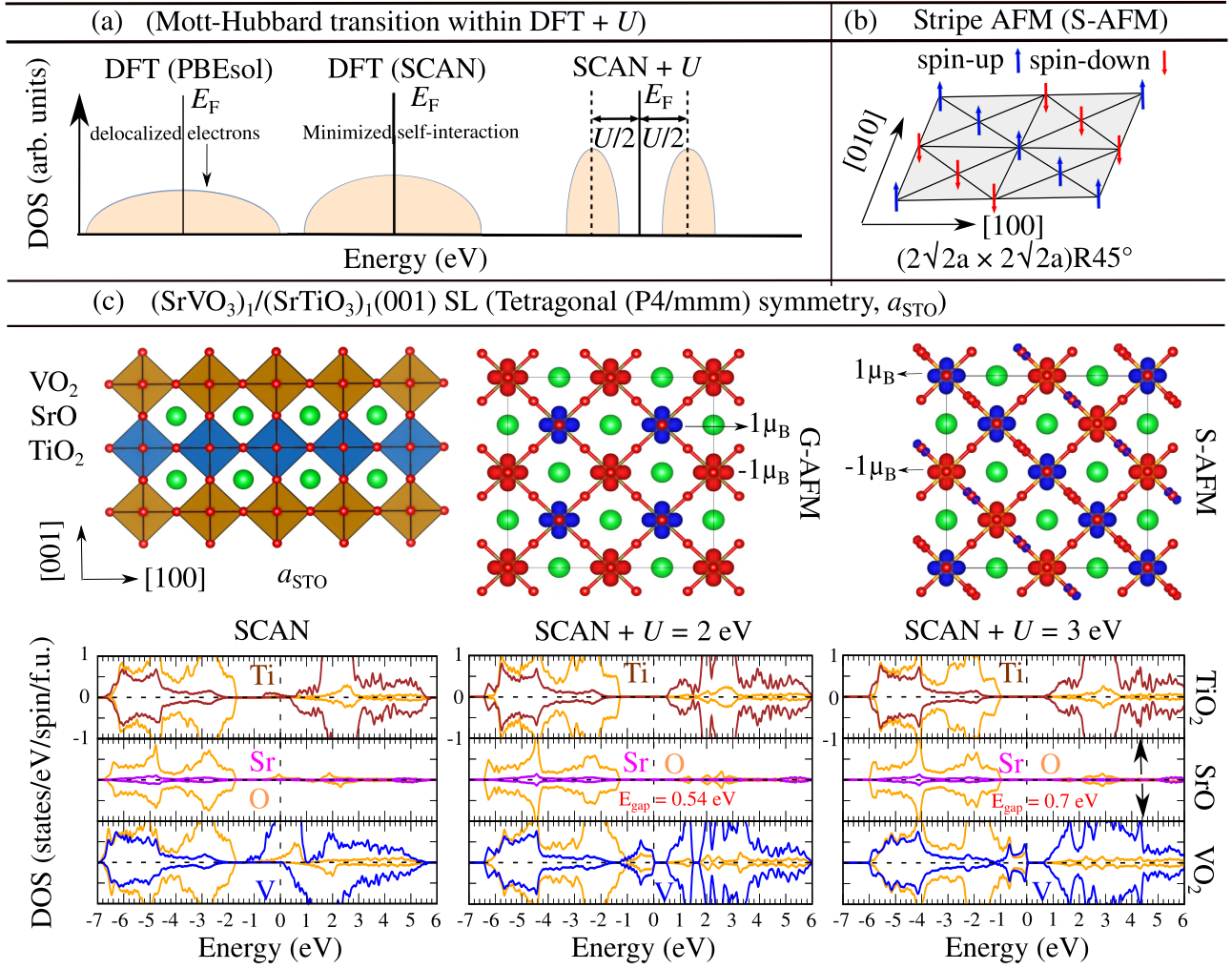


FIG. 6. (a) Diagrammatic representation of the minimization of the self-interaction error by SCAN functional, compared to PBEsol functional, and the subsequent Mott-Hubbard transition by SCAN + U , within the framework of the density functional theory. (b) 2D representation of the long-range AFM order (S-AFM) in a laterally enlarged $(2\sqrt{2}a \times 2\sqrt{2}a)R45^\circ$ SL, obtained by rotating the cubic perovskite unit cell by 45° about the [001] axis, having the lattice parameter a . (c) Top layer: side view of the optimized tetragonal $(\text{SrVO}_3)_1/(\text{SrTiO}_3)_1(001)$ SL ($P4/mmm$ symmetry) at a_{STO} , obtained from SCAN functional, along with the spin-density plots (integrated from -7 eV to the Fermi level (0 eV)); further show G- and S-type AFM order, and the site wise magnetic moments, at $U = 2$ and 3 eV, respectively. Bottom layer: layer-, element-, and spin-resolved densities of states of the tetragonal $(\text{SrVO}_3)_1/(\text{SrTiO}_3)_1(001)$ SLs ($P4/mmm$ symmetry) at a_{STO} , obtained from SCAN, SCAN + $U = 2$ eV and 3 eV, respectively. The PDOS have been averaged over all corresponding sites in a supercell and normalized to one SL formula unit. Blue and red colors in the integrated spin density plots represent the spin-up and spin-down channels, respectively. In the projected densities of states, the blue, magenta, orange and brown color represent V, Sr, O, and Ti states, respectively. The dashed line at the zero energy always represents the Fermi level.

MIT in $(\text{SVO})_1/(\text{STO})_1(001)$ SL at a_{YAO} . Further, a magnetic moment of $\sim 1\mu_B/\text{V}$ site was obtained in all the cases. Our finding of $3d_{xz}/d_{yz}$ orbitals quantization agrees with the recent DFT + DMFT reports of MIT in ultrathin confined SVO slab, caused by the quantization of V $3d_{xz}/d_{yz}$ orbitals (nonmagnetic), at compressive strain, as rendered by the $(\text{LaAlO}_3)_{0.3}(\text{Sr}_2\text{TaAlO}_6)_{0.7}$ (LSAT) substrate ($a = 3.868$ Å) [104,105].

Band alignments can be understood similarly as explained in section VI. From the layer-resolved density of states (Fig. 7) and the energy band structure diagrams (Fig. 8), we observe highly localized V $3d_{xz}/d_{yz}$ states (between -0.6 eV and E_F), at $U = 2$ and 3 eV, respectively, compared to the delocalized V $3d_{xz}/d_{yz}$ states crossing the Fermi energy, obtained from the SCAN functional.

IX. THERMOELECTRIC PROPERTIES OF $(\text{SrVO}_3)_1/(\text{SrTiO}_3)_1(001)$ SL

Finally, we discuss the thermoelectric properties of $(\text{SVO})_1/(\text{STO})_1(001)$ SL with the ground state orthorhombic ($Cmmm$) symmetry at a_{STO} , obtained from SCAN + U , $U = 3$ eV. We consider the energetically more favourable S-type AFM order at a_{STO} (see Fig. 3). In Fig. 9, we report power factors divided by the relaxation time PF/τ which are hence independent of the choice of τ and related to the electronic fitness function introduced by Xing *et al.* [106]. In Table III, we use a room-temperature relaxation time of $\tau = 4$ fs, a typical value for oxides [39,107]. In our discussion, we focus on chemical potential (μ) values within a physically relevant ± 100 meV interval around the band edges, highlighted with

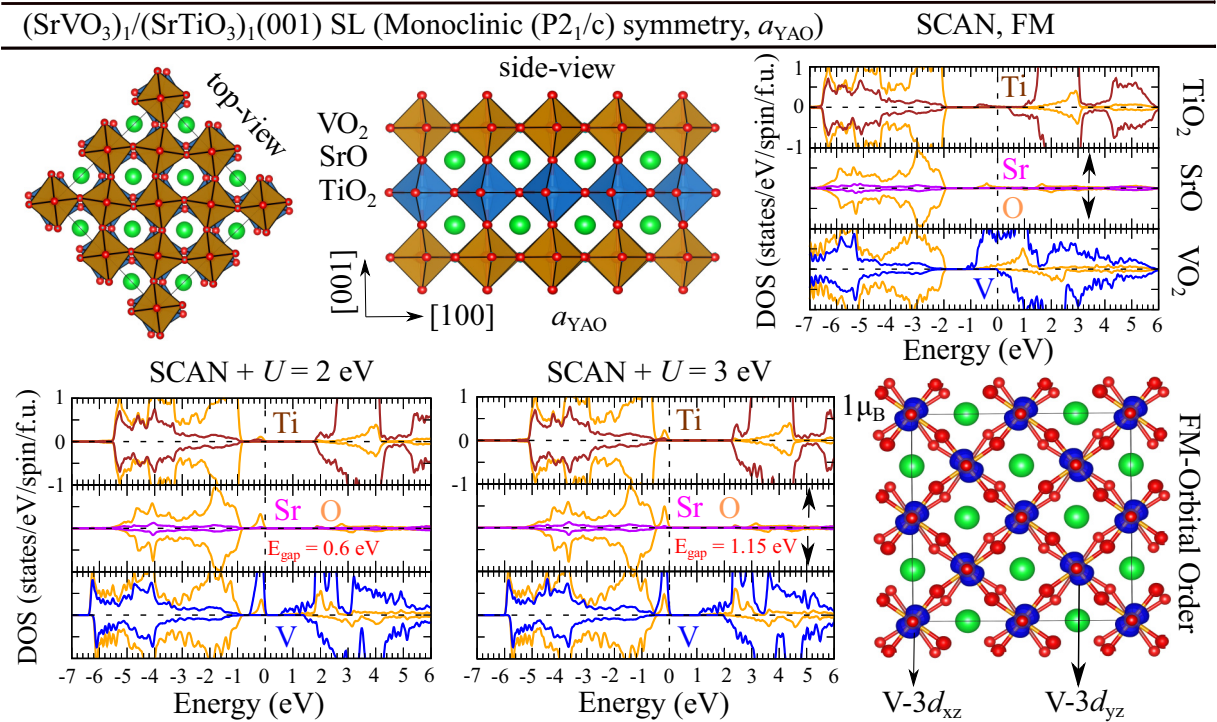


FIG. 7. (Top) Top and side views of the optimized monoclinic $(\text{SrVO}_3)_1/(\text{SrTiO}_3)_1(001)$ SL ($P2_1/c$ symmetry) at a_{YAO} , along with layer-, element-, and spin-resolved densities of states, obtained from SCAN functional. (Bottom) Layer-, element-, and spin-resolved densities of states, obtained from SCAN + $U = 2$ and 3 eV, respectively, along with the integrated spin-density plot (integrated from -7 eV to the Fermi level $[0$ eV]); further shows FM orbital-order, and the site wise magnetic moments, at $U = 3$ eV. The PDOS have been averaged over all corresponding sites in a supercell and normalized to one SL formula unit. Blue and red colors in the integrated spin density plots represent the spin-up and spin-down channels, respectively. In the projected densities of states, the blue, magenta, orange and brown color represent V, Sr, O, and Ti states, respectively. The dashed line at the zero energy represents the Fermi level.

cyan (around VBM) and magenta (CBM), respectively. The values in Table III refers to 300 K.

Analyzing the plots for thermoelectric quantities in the vicinity of the conduction band edge (n -type) (Fig. 9), we observe that the in-plane electrical conductivity σ/τ amounts to ~ 150 $1/\Omega$ cm fs, whereas the cross-plane electrical conductivity σ/τ reaches much higher values of ~ 300 $1/\Omega$ cm fs, due to the vacant $3d_{xz,yz}$ orbitals in both the spin channels. Moreover, confinement and correlation driven band gap opening (0.73 eV) lead to high Seebeck coefficients S of -566 (in-plane) and -454 $\mu\text{V}/\text{K}$ (cross-plane), respectively, at

300 K. The high S and high σ give rise to promising in-plane (cross-plane) power factor (PF) of 31.4 (8.5) $\mu\text{W}/\text{K}^2$ cm (assuming $\tau = 4$ fs) at 300 K. Notably, different in-plane and cross-plane thermoelectric quantities result due to anisotropy arising from the layered crystal structure of the $1/1$ SL.

Next, the total figure of merit is calculated as $ZT|_{\text{tot.}} = \frac{TS^2\sigma}{\kappa_e + \kappa_l}$, where κ_e and κ_l are the electronic and lattice thermal conductivities, respectively. Theoretical calculation of lattice thermal conductivity involves the demanding calculation of anharmonic contributions which is beyond the scope of this work. Recently, Katsufuji *et al.* [26] experimentally measured

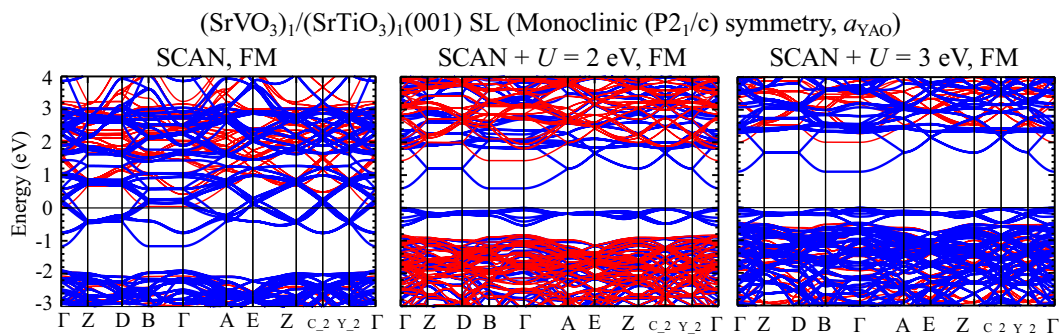


FIG. 8. Band structure diagrams of the monoclinic $(\text{SrVO}_3)_1/(\text{SrTiO}_3)_1(001)$ SL ($P2_1/c$ symmetry) at a_{YAO} , obtained from SCAN, SCAN + $U = 2$ and 3 eV, respectively. Blue and red bands correspond to spin-up and spin-down channels, respectively.

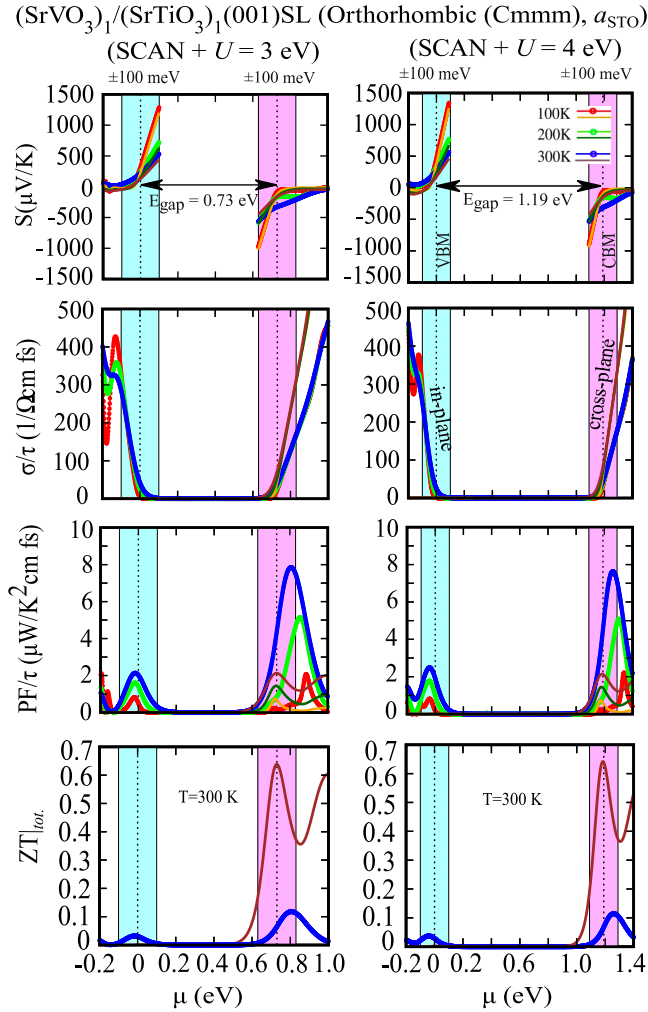


FIG. 9. Thermoelectric properties of the orthorhombic $(\text{SrVO}_3)_1/(\text{SrTiO}_3)_1(001)$ SL (C_{mmm} symmetry) at a_{STO} , obtained from SCAN + $U = 3$ and 4 eV, respectively. Three different temperatures are displayed for each thermoelectric quantity (except ZT): 100, 200, and 300 K. (Left to right) Seebeck coefficient S , power factor PF/τ , electrical conductivity σ/τ , and the total figure of merit $ZT|_{\text{tot}}$, respectively are shown, where τ denotes the relaxation time. Orange, dark-green, and brown lines (red, green, and blue lines with points) correspond to cross-plane (in-plane) transport. The vertical dashed line at zero energy denotes the VBM; the second vertical dashed line indicates the CBM. The energy windows of physical importance (± 100 meV) are marked in cyan (around VBM) and magenta (around CBM) colors, respectively.

the thermal conductivity of $(\text{SVO})_n/(\text{STO})_n(001)$ multilayer thin films normal to the surface by varying the thickness n , with thermal conductivity reaching as low as 0.4 W/m K for $n = 10$ nm. In the following we adopt this value to estimate the out-of-plane $ZT|_{\text{tot}}$ in the 1/1 SL at a_{STO} . Note that the distinct contributions from κ_e and κ_l are not known in the experimentally measured thermal conductivity. Hence in our calculation of $ZT|_{\text{tot}}$ we have ignored the electronic part of thermal conductivity obtained from DFT + U . To calculate the in-plane value of $ZT|_{\text{tot}}$ in the 1/1 SL, we adopt the experimentally reported thermal conductivity value of 8 W/m K for SVO film (70 nm) as the high thermal resistance was

TABLE III. Comparison of the attainable thermoelectric performance of the present system (Fig. 9) using SCAN + $U = 3$ eV and to a selection of prominent oxide thermoelectrics at room temperature (300 K).

System	S ($\mu\text{V}/\text{K}$)	PF ($\mu\text{W K}^{-2} \text{cm}^{-1}$)	$ZT _{\text{tot}}$
(SVO) ₁ /(STO) ₁ (001) SL, (this work, $\tau = 4$ fs)			
In-plane (xx)	-566	31.4	0.12
Cross-plane (zz)	-454	8.5	0.64
(LNO) ₁ /(LAO) ₁ (001) SL [39]			
In-plane (xx)	-600	11	-
Cross-plane (zz)	-600	2	-
SrTiO ₃ (DFT [107])	-400	10	-
La:SrTiO ₃ bulk, exp. [108]	-380	35	0.09
La:SrTiO ₃ films, exp. [109]	-980	39	-
Nb:SrTiO ₃ bulk, exp. [110]	-240	20	0.06

reported only across the interface [26]. From the $ZT|_{\text{tot}}$ plot in Fig. 9, we obtain the approximate in-plane (cross-plane) values of 0.12 (0.64), reaching beyond the ZT values of 0.09 in La-doped STO [108] and 0.06 in Nb-doped STO [110] at 300 K. Our estimated cross-plane value of $ZT|_{\text{tot}}$ (0.64) can be compared directly with the value of 0.24 reported for $\text{SrTi}_{0.8}\text{Nb}_{0.2}\text{O}_3/\text{STO}$ SLs [111] at 300 K. A more detailed comparison of thermoelectric quantities with respect to other high-performing oxide thermoelectrics can be found in the Table III. Lastly, it can be argued that the values of S , PF, and $ZT|_{\text{tot}}$ calculated for the 1/1 SL depend on the choice of Hubbard U term. To substantiate our thermoelectric results, we performed additional calculations using SCAN + U , $U = 4$ eV for $(\text{SVO})_1/(\text{STO})_1(001)$ SL at a_{STO} having orthorhombic (C_{mmm}) symmetry. From Fig. 9 (panels on the right side), it can be observed that except for the larger band gap of 1.19 eV, the thermoelectric response at the CBE and VBE remains qualitatively unchanged. We obtain the in-plane (cross-plane) Seebeck coefficients of -535 $\mu\text{V}/\text{K}$ (-432 $\mu\text{V}/\text{K}$), PF of 30.6 $\mu\text{W K}^{-2} \text{cm}^{-1}$ (8.6 $\mu\text{W K}^{-2} \text{cm}^{-1}$) (assuming $\tau = 4$ fs), and $ZT|_{\text{tot}}$ of 0.11 (0.64), respectively, with SCAN + U , $U = 4$ eV, close to the results obtained with SCAN + U , $U = 3$ eV.

X. SUMMARY

To summarize, based on the density functional theory calculations combined with an on-site Coulomb repulsion term U for $(\text{SrXO}_3)_1/(\text{SrTiO}_3)_1(001)$ superlattice (SLs), $X = \text{V}$, and Ru, we have outlined a general recipe to address the electronic and magnetic properties using the correct ground state structural symmetry, at a given in-plane lattice constant. We have demonstrated that the meta GGA SCAN functional correctly describes the structural properties and is already sufficient to address the electronic and magnetic properties of the weakly correlated $(\text{SrRuO}_3)_1/(\text{SrTiO}_3)_1(001)$ SL and its bulk constituents by minimizing the self-interaction error. In contrast, an additional on-site Coulomb repulsion term is necessary to describe the electronic and magnetic properties of the correlated bulk SrVO_3 as well as in $(\text{SrVO}_3)_1/(\text{SrTiO}_3)_1(001)$ SLs. Based on

the structural symmetries of $(\text{SrVO}_3)_1/(\text{SrTiO}_3)_1(001)$ SLs at the in-plane lattice constants of bulk STO and YAO, respectively, determined with the SCAN functional, we report distinct mechanisms of the metal-to-insulator transition in the $(\text{SrVO}_3)_1/(\text{SrTiO}_3)_1(001)$ SLs. Using Boltzmann transport theory within the constant relaxation time approximation for $(\text{SrVO}_3)_1/(\text{SrTiO}_3)_1(001)$ SL at the in-plane lattice constant of bulk STO, we have obtained a robust thermoelectric response categorizing it among the prominent oxide thermoelectric materials. The results presented here to study strongly correlated quantum phases while incorporating realistic structural degrees of freedom might be instructive for other, not limited to SrTiO_3 , based superlattices and heterostructures.

ACKNOWLEDGMENTS

This work was supported by the German Research Foundation (Deutsche Forschungsgemeinschaft, DFG) within the SFB/TRR 80 (Projektnummer 107745057, subprojects G3 and G8). We acknowledge computational time at the Leibniz Rechenzentrum Garching, Project No. pr87ro and magnetUDE supercomputer (DFG Grants No. INST 20876/209-1 FUGG and No. INST 20876/243-1 FUGG). M.V. acknowledges fruitful discussions with Alex Zunger at University of Colorado Boulder. We acknowledge support by the Open Access Publication fund of the University of Duisburg-Essen.

- [1] J. Mannhart and D. G. Schlom, Oxide interfaces—an opportunity for electronics, *Science* **327**, 1607 (2010).
- [2] A. V. Boris, Y. Matiks, E. Benckiser, A. Frano, P. Popovich, V. Hinkov, P. Wochner, M. Castro-Colin, E. Detemple, V. K. Malik, C. Bernhard, T. Prokscha, A. Suter, Z. Salman, E. Morenzoni, G. Cristiani, H.-U. Habermeyer, and B. Keimer, Dimensionality control of electronic phase transitions in nickel-oxide superlattices, *Science* **332**, 937 (2011).
- [3] Y. Lan, X. Chen, and M. He, Structure, magnetic susceptibility and resistivity properties of SrVO_3 , *J. Alloys Compd.* **354**, 95 (2003).
- [4] J. A. Moyer, C. Eaton, and R. Engel-Herbert, Highly conductive SrVO_3 as a bottom electrode for functional perovskite oxides, *Adv. Mater.* **25**, 3578 (2013).
- [5] K. Yoshimatsu, T. Okabe, H. Kumigashira, S. Okamoto, S. Aizaki, A. Fujimori, and M. Oshima, Dimensional-Crossover-Driven Metal-Insulator Transition in SrVO_3 Ultrathin Films, *Phys. Rev. Lett.* **104**, 147601 (2010).
- [6] M. Gu, S. A. Wolf, and J. Lu, Two-dimensional mott insulators in SrVO_3 ultrathin films, *Adv. Mater. Interfaces* **1**, 1300126 (2014).
- [7] A. Fouchet, M. Allain, B. Bérini, E. Popova, P.-E. Janolin, N. Guiblin, E. Chikoidze, J. Scola, D. Hrabovsky, Y. Dumont, and N. Keller, Study of the electronic phase transition with low dimensionality in SrVO_3 thin films, *Mater. Sci. Eng. B* **212**, 7 (2016).
- [8] J. Wang, N. Gauquelin, M. Huijben, J. Verbeeck, G. Rijnders, and G. Koster, Metal-insulator transition of SrVO_3 ultrathin films embedded in $\text{SrVO}_3/\text{SrTiO}_3$ superlattices, *Appl. Phys. Lett.* **117**, 133105 (2020).
- [9] V. Pardo and W. E. Pickett, Electron confinement, orbital ordering, and orbital moments in d^0-d^1 oxide heterostructures, *Phys. Rev. B* **81**, 245117 (2010).
- [10] H. Kawano, H. Yoshizawa, and Y. Ueda, Magnetic Behavior of a Mott-Insulator YVO_3 , *J. Phys. Soc. Jpn.* **63**, 2857 (1994).
- [11] M. Noguchi, A. Nakazawa, S. Oka, T. Arima, Y. Wakabayashi, H. Nakao, and Y. Murakami, Synchrotron x-ray-diffraction study of orbital ordering in YVO_3 , *Phys. Rev. B* **62**, R9271 (2000).
- [12] G. R. Blake, T. T. M. Palstra, Y. Ren, A. A. Nugroho, and A. A. Menovsky, Transition between Orbital Orderings in YVO_3 , *Phys. Rev. Lett.* **87**, 245501 (2001).
- [13] S. Miyasaka, Y. Okimoto, and Y. Tokura, Anisotropy of Mott-Hubbard gap transitions due to spin and orbital ordering in LaVO_3 and YVO_3 , *J. Phys. Soc. Jpn.* **71**, 2086 (2002).
- [14] M. Verma, B. Geisler, and R. Pentcheva, Effect of confinement and octahedral rotations on the electronic, magnetic, and thermoelectric properties of correlated $\text{SrXO}_3/\text{SrTiO}_3(001)$ superlattices ($X = \text{V, Cr, or Mn}$), *Phys. Rev. B* **100**, 165126 (2019).
- [15] J. M. Rondinelli and N. A. Spaldin, Electron-lattice instabilities suppress cuprate-like electronic structures in $\text{SrFeO}_3/\text{SrTiO}_3$ superlattices, *Phys. Rev. B* **81**, 085109 (2010).
- [16] J. M. Rondinelli and N. A. Spaldin, Substrate coherency driven octahedral rotations in perovskite oxide films, *Phys. Rev. B* **82**, 113402 (2010).
- [17] J. Varignon, M. Bibes, and A. Zunger, Origin of band gaps in 3d perovskite oxides, *Nat. Commun.* **10**, 1658 (2019).
- [18] W. Kohn and L. J. Sham, Self-consistent equations including exchange and correlation effects, *Phys. Rev.* **140**, A1133 (1965).
- [19] S. L. Dudarev, G. A. Botton, S. Y. Savrasov, C. J. Humphreys, and A. P. Sutton, Electron-energy-loss spectra and the structural stability of nickel oxide: An LSDA+U study, *Phys. Rev. B* **57**, 1505 (1998).
- [20] N. W. Ashcroft and N. D. Mermin, *Solid State Physics* (Holt-Saunders, 1976).
- [21] J. Hubbard and B. H. Flowers, Electron correlations in narrow energy bands, *Proc. R. Soc. London A* **276**, 238 (1963).
- [22] J. Hubbard and B. H. Flowers, Electron correlations in narrow energy bands III. An improved solution, *Proc. R. Soc. London A* **281**, 401 (1964).
- [23] M. Pickem, J. Kaufmann, K. Held, and J. M. Tomczak, Zoology of spin and orbital fluctuations in ultrathin oxide films, *Phys. Rev. B* **104**, 024307 (2021).
- [24] I. I. Mazin, D. I. Khomskii, R. Lengsdorf, J. A. Alonso, W. G. Marshall, R. M. Ibberson, A. Podlesnyak, M. J. Martínez-Lope, and M. M. Abd-Elmeguid, Charge Ordering as Alternative to Jahn-Teller Distortion, *Phys. Rev. Lett.* **98**, 176406 (2007).
- [25] M. Mirjolet, H. B. Vasili, A. Valadkhani, J. Santiso, V. Borisov, P. Gargiani, M. Valdivares, R. Valentí, and J. Fontcuberta, Orbital occupancy and hybridization in strained SrVO_3 epitaxial films, *Phys. Rev. Materials* **5**, 095002 (2021).
- [26] T. Katsufuji, T. Saiki, S. Okubo, Y. Katayama, and K. Ueno, Thermal conductivity of SrVO_3 - SrTiO_3 thin films: Evidence of intrinsic thermal resistance at the interface between oxide layers, *Phys. Rev. Materials* **2**, 051002(R) (2018).
- [27] J. P. Perdew, A. Ruzsinszky, G. I. Csonka, O. A. Vydrov, G. E. Scuseria, L. A. Constantin, X. Zhou, and K. Burke, Restoring

- the Density-Gradient Expansion for Exchange in Solids and Surfaces, *Phys. Rev. Lett.* **100**, 136406 (2008).
- [28] J. Sun, A. Ruzsinszky, and J. P. Perdew, Strongly Constrained and Appropriately Normed Semilocal Density Functional, *Phys. Rev. Lett.* **115**, 036402 (2015).
- [29] G. Kresse and J. Hafner, Ab initio molecular dynamics for liquid metals, *Phys. Rev. B* **47**, 558 (1993).
- [30] G. Kresse and J. Furthmüller, Efficient iterative schemes for ab initio total-energy calculations using a plane-wave basis set, *Phys. Rev. B* **54**, 11169 (1996).
- [31] P. E. Blöchl, Projector augmented-wave method, *Phys. Rev. B* **50**, 17953 (1994).
- [32] G. Kresse and D. Joubert, From ultrasoft pseudopotentials to the projector augmented-wave method, *Phys. Rev. B* **59**, 1758 (1999).
- [33] H. J. Monkhorst and J. D. Pack, Special points for Brillouin-zone integrations, *Phys. Rev. B* **13**, 5188 (1976).
- [34] G. K. Madsen and D. J. Singh, Boltztrap. a code for calculating band-structure dependent quantities, *Comput. Phys. Commun.* **175**, 67 (2006).
- [35] U. Sivan and Y. Imry, Multichannel Landauer formula for thermoelectric transport with application to thermopower near the mobility edge, *Phys. Rev. B* **33**, 551 (1986).
- [36] L. K. Lamontagne, G. Laurita, M. W. Gaultois, M. Knight, L. Ghadbeigi, T. D. Sparks, M. E. Gruner, R. Pentcheva, C. M. Brown, and R. Seshadri, High thermopower with metallic conductivity in p-type Li-substituted PbPdO₂, *Chem. Mater.* **28**, 3367 (2016).
- [37] M. E. Gruner, U. Eckern, and R. Pentcheva, Impact of strain-induced electronic topological transition on the thermoelectric properties of PtCoO₂ and PdCoO₂, *Phys. Rev. B* **92**, 235140 (2015).
- [38] B. Geisler, A. Blanca-Romero, and R. Pentcheva, Design of *n*- and *p*-type oxide thermoelectrics in LaNiO₃/SrTiO₃(001) superlattices exploiting interface polarity, *Phys. Rev. B* **95**, 125301 (2017).
- [39] B. Geisler and R. Pentcheva, Confinement- and strain-induced enhancement of thermoelectric properties in LaNiO₃/LaAlO₃(001) superlattices, *Phys. Rev. Materials* **2**, 055403 (2018).
- [40] B. Geisler and R. Pentcheva, Inducing *n*- and *p*-type Thermoelectricity in Oxide Superlattices by Strain Tuning of Orbital-Selective Transport Resonances, *Phys. Rev. Appl.* **11**, 044047 (2019).
- [41] B. Geisler and P. Kratzer, Spin-caloric properties of epitaxial Co₂MnSi/MgO/Co₂MnSi magnetic junctions, *Phys. Rev. B* **92**, 144418 (2015).
- [42] B. Geisler, P. Kratzer, and V. Popescu, Interplay of growth mode and thermally induced spin accumulation in epitaxial Al/Co₂TiSi/Al and Al/Co₂TiGe/Al contacts, *Phys. Rev. B* **89**, 184422 (2014).
- [43] D. Comtesse, B. Geisler, P. Entel, P. Kratzer, and L. Szunyogh, First-principles study of spin-dependent thermoelectric properties of half-metallic Heusler thin films between platinum leads, *Phys. Rev. B* **89**, 094410 (2014).
- [44] P. Giannozzi, S. Baroni, N. Bonini, M. Calandra, R. Car, C. Cavazzoni, D. Ceresoli, G. L. Chiarotti, M. Cococcioni, I. Dabo, A. D. Corso, S. de Gironcoli, S. Fabris, G. Fratesi, R. Gebauer, U. Gerstmann, C. Gougoussis, A. Kokalj, M. Lazzeri, L. Martin-Samos *et al.*, Quantum Espresso: a modular and open-source software project for quantum simulations of materials, *J. Phys.: Condens. Matter* **21**, 395502 (2009).
- [45] P. Giannozzi, O. Andreussi, T. Brumme, O. Bunau, M. B. Nardelli, M. Calandra, R. Car, C. Cavazzoni, D. Ceresoli, M. Cococcioni, N. Colonna, I. Carnimeo, A. D. Corso, S. de Gironcoli, P. Delugas, R. A. DiStasio, A. Ferretti, A. Floris, G. Fratesi, G. Fugallo *et al.*, Advanced capabilities for materials modelling with Quantum Espresso, *J. Phys.: Condens. Matter* **29**, 465901 (2017).
- [46] P. Giannozzi, O. Baseggio, P. Bonfà, D. Brunato, R. Car, I. Carnimeo, C. Cavazzoni, S. de Gironcoli, P. Delugas, F. Ferrari Ruffino, A. Ferretti, N. Marzari, I. Timrov, A. Urru, and S. Baroni, Quantum Espresso toward the exascale, *J. Chem. Phys.* **152**, 154105 (2020).
- [47] A. Dal Corso, Pseudopotentials periodic table: From H to Pu, *Comput. Mater. Sci.* **95**, 337 (2014).
- [48] I. Timrov, F. Aquilante, L. Binci, M. Cococcioni, and N. Marzari, Pulay forces in density-functional theory with extended Hubbard functionals: From nonorthogonalized to orthogonalized manifolds, *Phys. Rev. B* **102**, 235159 (2020).
- [49] M. Cococcioni and S. de Gironcoli, Linear response approach to the calculation of the effective interaction parameters in the LDA + U method, *Phys. Rev. B* **71**, 035105 (2005).
- [50] I. Timrov, N. Marzari, and M. Cococcioni, Hubbard parameters from density-functional perturbation theory, *Phys. Rev. B* **98**, 085127 (2018).
- [51] J. Garcíá-Jaca, J. Mesa, M. Insausti, J. Larramendi, M. Arriortua, and T. Rojo, Synthesis, crystal structure, stoichiometry and magnetic properties of (Ca_{1-x}Sr_x)VO₃, *Mater. Res. Bull.* **34**, 289 (1999).
- [52] C. W. Jones, P. D. Battle, P. Lightfoot, and W. T. A. Harrison, The structure of SrRuO₃ by time-of-flight neutron powder diffraction, *Acta Crystallogr. Sect. C* **45**, 365 (1989).
- [53] A. Kanbayasi, Magnetic properties of SrRuO₃ single crystal, *J. Phys. Soc. Jpn.* **41**, 1876 (1976).
- [54] J. M. Rondinelli, N. M. Caffrey, S. Sanvito, and N. A. Spaldin, Electronic properties of bulk and thin film SrRuO₃: Search for the metal-insulator transition, *Phys. Rev. B* **78**, 155107 (2008).
- [55] M. Verissimo-Alves, P. García-Fernández, D. I. Bilc, P. Ghosez, and J. Junquera, Highly Confined Spin-Polarized Two-Dimensional Electron Gas in SrTiO₃/SrRuO₃ Superlattices, *Phys. Rev. Lett.* **108**, 107003 (2012).
- [56] M. Gu, Q. Xie, X. Shen, R. Xie, J. Wang, G. Tang, D. Wu, G. P. Zhang, and X. S. Wu, Magnetic Ordering and Structural Phase Transitions in a Strained Ultrathin SrRuO₃/SrTiO₃ Superlattice, *Phys. Rev. Lett.* **109**, 157003 (2012).
- [57] F. Bern, M. Ziese, A. Setzer, E. Pippel, D. Hesse, and I. Vrejoiu, Structural, magnetic and electrical properties of SrRuO₃ films and SrRuO₃/SrTiO₃ superlattices, *J. Phys.: Condens. Matter* **25**, 496003 (2013).
- [58] W. Lu, P. Yang, W. D. Song, G. M. Chow, and J. S. Chen, Control of oxygen octahedral rotations and physical properties in SrRuO₃ films, *Phys. Rev. B* **88**, 214115 (2013).
- [59] S. Pang, Review on electronic correlations and the metal-insulator transition in SrRuO₃, *Appl. Microsc.* **47**, 187 (2017).
- [60] H. Boschker, T. Harada, T. Asaba, R. Ashoori, A. V. Boris, H. Hilgenkamp, C. R. Hughes, M. E. Holtz, L. Li, D. A. Muller, H. Nair, P. Reith, X. Renshaw Wang, D. G. Schlom, A. Soukiassian, and J. Mannhart, Ferromagnetism and

- Conductivity in Atomically Thin SrRuO₃, *Phys. Rev. X* **9**, 011027 (2019).
- [61] K. Maiti and R. S. Singh, Evidence against strong correlation in 4d transition-metal oxides CaRuO₃ and SrRuO₃, *Phys. Rev. B* **71**, 161102(R) (2005).
- [62] G. Trimarchi, Z. Wang, and A. Zunger, Polymorphous band structure model of gapping in the antiferromagnetic and paramagnetic phases of the Mott insulators MnO, FeO, CoO, and NiO, *Phys. Rev. B* **97**, 035107 (2018).
- [63] J. Varignon, M. N. Grisolia, D. Preziosi, P. Ghosez, and M. Bibes, Origin of the orbital and spin ordering in rare-earth titanates, *Phys. Rev. B* **96**, 235106 (2017).
- [64] J. Varignon, M. N. Grisolia, J. Íñiguez, A. Barthélémy, and M. Bibes, Complete phase diagram of rare-earth nickelates from first-principles, *npj Quantum Mater.* **2**, 21 (2017).
- [65] J. Varignon, N. C. Bristowe, E. Bousquet, and P. Ghosez, Coupling and electrical control of structural, orbital and magnetic orders in perovskites, *Sci. Rep.* **5**, 15364 (2015).
- [66] A. Mercy, J. Bieder, J. Íñiguez, and P. Ghosez, Structurally triggered metal-insulator transition in rare-earth nickelates, *Nat. Commun.* **8**, 1677 (2017).
- [67] A. Cammarata and J. M. Rondinelli, Spin-assisted covalent bond mechanism in “charge-ordering” perovskite oxides, *Phys. Rev. B* **86**, 195144 (2012).
- [68] Y. Zhang, M. M. Schmitt, A. Mercy, J. Wang, and P. Ghosez, From charge- to orbital-ordered metal-insulator transition in alkaline-earth ferrites, *Phys. Rev. B* **98**, 081108(R) (2018).
- [69] Z. Zanolli, J. C. Wojdet, J. Íñiguez, and P. Ghosez, Electric control of the magnetization in BiFeO₃/LaFeO₃ superlattices, *Phys. Rev. B* **88**, 060102(R) (2013).
- [70] T. A. Mellan, F. Corà, R. Grau-Crespo, and S. Ismail-Beigi, Importance of anisotropic Coulomb interaction in LaMnO₃, *Phys. Rev. B* **92**, 085151 (2015).
- [71] J. Sun, R. C. Remsing, Y. Zhang, Z. Sun, A. Ruzsinszky, H. Peng, Z. Yang, A. Paul, U. Waghmare, X. Wu, M. L. Klein, and J. P. Perdew, Accurate first-principles structures and energies of diversely bonded systems from an efficient density functional, *Nat. Chem.* **8**, 831 (2016).
- [72] J. Varignon, M. Bibes, and A. Zunger, Mott gapping in 3dABO₃ perovskites without Mott-Hubbard interelectronic repulsion energy U, *Phys. Rev. B* **100**, 035119 (2019).
- [73] Y. Zhang, J. Furness, R. Zhang, Z. Wang, A. Zunger, and J. Sun, Symmetry-breaking polymorphous descriptions for correlated materials without interelectronic U, *Phys. Rev. B* **102**, 045112 (2020).
- [74] C. Lane, J. W. Furness, I. G. Buda, Y. Zhang, R. S. Markiewicz, B. Barbiellini, J. Sun, and A. Bansil, Antiferromagnetic ground state of La₂ CuO₄: A parameter-free ab initio description, *Phys. Rev. B* **98**, 125140 (2018).
- [75] Y. Fu and D. J. Singh, Density functional methods for the magnetism of transition metals: Scan in relation to other functionals, *Phys. Rev. B* **100**, 045126 (2019).
- [76] See Supplemental Material at <http://link.aps.org/supplemental/10.1103/PhysRevResearch.4.033013> for structural parameters of (SrXO₃)₁/(SrTiO₃)₁(001), X = V, Ru, superlattices, discussion on spin-orbit coupling in bulk SrRuO₃ and (SrRuO₃)₁/(SrTiO₃)₁(001) superlattices, additional discussion on electronic and magnetic properties of (SrVO₃)₁/(SrTiO₃)₁(001) superlattices having monoclinic (P2₁/c) symmetry at a_{STO}, electronic properties of bulk SrTiO₃, and orbital projected density of states of bulk SrRuO₃ and (SrXO₃)₁/(SrTiO₃)₁(001), X = V, Ru, superlattices.
- [77] V. Begum, M. E. Gruner, and R. Pentcheva, Role of the exchange-correlation functional on the structural, electronic, and optical properties of cubic and tetragonal SrTiO₃ including many-body effects, *Phys. Rev. Materials* **3**, 065004 (2019).
- [78] A. Huang, H.-T. Jeng, and C.-H. Chang, First-principles calculations predict tunable large magnetic anisotropy due to spin-polarized quantum-well resonances in nanometer-thick SrRuO₃ films: Implications for spintronic devices, *ACS Appl. Nano Mater.* **4**, 5932 (2021).
- [79] D. Tian, Z. Liu, S. Shen, Z. Li, Y. Zhou, H. Liu, H. Chen, and P. Yu, Manipulating berry curvature of SrRuO₃ thin films via epitaxial strain, *Proc. Natl. Acad. Sci. USA* **118**, e2101946118 (2021).
- [80] K. Samanta, M. Ležaić, M. Merte, F. Freimuth, S. Blügel, and Y. Mokrousov, Crystal hall and crystal magneto-optical effect in thin films of SrRuO₃, *J. Appl. Phys.* **127**, 213904 (2020).
- [81] A. J. Grutter, F. J. Wong, E. Arenholz, A. Vailionis, and Y. Suzuki, Evidence of high-spin ru and universal magnetic anisotropy in SrRuO₃ thin films, *Phys. Rev. B* **85**, 134429 (2012).
- [82] S. G. Jeong, H. Kim, S. J. Hong, D. Suh, and W. S. Choi, Symmetry-driven spin-wave gap modulation in nanolayered SrRuO₃/SrTiO₃ heterostructures: Implications for spintronic applications, *ACS Appl. Nano Mater.* **4**, 2160 (2021).
- [83] Z. Cui, A. J. Grutter, H. Zhou, H. Cao, Y. Dong, D. A. Gilbert, J. Wang, Y.-S. Liu, J. Ma, Z. Hu, J. Guo, J. Xia, B. J. Kirby, P. Shafer, E. Arenholz, H. Chen, X. Zhai, and Y. Lu, Correlation-driven eightfold magnetic anisotropy in a two-dimensional oxide monolayer, *Sci. Adv.* **6**, eaay0114 (2020).
- [84] T. Maekawa, K. Kurosaki, and S. Yamanaka, Physical properties of polycrystalline SrVO_{3-δ}, *J. Alloys Compd.* **426**, 46 (2006).
- [85] B. Chamberland and P. Danielson, Alkaline-earth vanadium (IV) oxides having the AVO₃ composition, *J. Solid State Chem.* **3**, 243 (1971).
- [86] P. Dougier, J. C. Fan, and J. B. Goodenough, Etude des proprietes magnetiques, electriques et optiques des phases de structure perovskite SrVO_{2.90} et SrVO₃, *J. Solid State Chem.* **14**, 247 (1975).
- [87] M. Onoda, H. Ohta, and H. Nagasawa, Metallic properties of perovskite oxide SrVO₃, *Solid State Commun.* **79**, 281 (1991).
- [88] V. Giannakopoulou, P. Odier, J. Bassat, and J. Loup, SrVO₃ and Sr₂VO₄, electrical properties below and above room T, *Solid State Commun.* **93**, 579 (1995).
- [89] K. Morikawa, T. Mizokawa, K. Kobayashi, A. Fujimori, H. Eisaki, S. Uchida, F. Iga, and Y. Nishihara, Spectral weight transfer and mass renormalization in mott-hubbard systems SrVO₃ and CaVO₃: Influence of long-range coulomb interaction, *Phys. Rev. B* **52**, 13711 (1995).
- [90] I. H. Inoue, O. Goto, H. Makino, N. E. Hussey, and M. Ishikawa, Bandwidth control in a perovskite-type 3d¹-correlated metal Ca_{1-x}Sr_xVO₃ I. evolution of the electronic properties and effective mass, *Phys. Rev. B* **58**, 4372 (1998).
- [91] A. Sekiyama, H. Fujiwara, S. Imada, S. Suga, H. Eisaki, S. I. Uchida, K. Takegahara, H. Harima, Y. Saitoh, I. A. Nekrasov, G. Keller, D. E. Kondakov, A. V. Kozhevnikov, T. Pruschke, K. Held, D. Vollhardt, and V. I. Anisimov, Mutual Experiment-

- tal and Theoretical Validation of Bulk Photoemission Spectra of $\text{Sr}_{1-x}\text{Ca}_x\text{VO}_3$, *Phys. Rev. Lett.* **93**, 156402 (2004).
- [92] T. Yoshida, K. Tanaka, H. Yagi, A. Ino, H. Eisaki, A. Fujimori, and Z.-X. Shen, Direct Observation of the Mass Renormalization in SrVO_3 by Angle Resolved Photoemission Spectroscopy, *Phys. Rev. Lett.* **95**, 146404 (2005).
- [93] R. Eguchi, T. Kiss, S. Tsuda, T. Shimojima, T. Mizokami, T. Yokoya, A. Chainani, S. Shin, I. H. Inoue, T. Togashi, S. Watanabe, C. Q. Zhang, C. T. Chen, M. Arita, K. Shimada, H. Namatame, and M. Taniguchi, Bulk- and Surface-Sensitive High-Resolution Photoemission Study of Two Mott-Hubbard Systems: SrVO_3 and CaVO_3 , *Phys. Rev. Lett.* **96**, 076402 (2006).
- [94] M. Takizawa, M. Minohara, H. Kumigashira, D. Toyota, M. Oshima, H. Wadati, T. Yoshida, A. Fujimori, M. Lippmaa, M. Kawasaki, H. Koinuma, G. Sordi, and M. Rozenberg, Coherent and incoherent d band dispersions in SrVO_3 , *Phys. Rev. B* **80**, 235104 (2009).
- [95] T. Yoshida, M. Hashimoto, T. Takizawa, A. Fujimori, M. Kubota, K. Ono, and H. Eisaki, Mass renormalization in the bandwidth-controlled mott-hubbard systems SrVO_3 and CaVO_3 studied by angle-resolved photoemission spectroscopy, *Phys. Rev. B* **82**, 085119 (2010).
- [96] K. Yoshimatsu, K. Horiba, H. Kumigashira, T. Yoshida, A. Fujimori, and M. Oshima, Metallic quantum well states in artificial structures of strongly correlated oxide, *Science* **333**, 319 (2011).
- [97] S. Aizaki, T. Yoshida, K. Yoshimatsu, M. Takizawa, M. Minohara, S. Ideta, A. Fujimori, K. Gupta, P. Mahadevan, K. Horiba, H. Kumigashira, and M. Oshima, Self-Energy on the Low- to High-Energy Electronic Structure of Correlated Metal SrVO_3 , *Phys. Rev. Lett.* **109**, 056401 (2012).
- [98] D. Puggioni, A. Filippetti, and V. Fiorentini, Ordering and multiple phase transitions in ultrathin nickelate superlattices, *Phys. Rev. B* **86**, 195132 (2012).
- [99] S. S. A. Seo, M. J. Han, G. W. J. Hassink, W. S. Choi, S. J. Moon, J. S. Kim, T. Susaki, Y. S. Lee, J. Yu, C. Bernhard, H. Y. Hwang, G. Rijnders, D. H. A. Blank, B. Keimer, and T. W. Noh, Two-Dimensional Confinement of $3d^1$ Electrons in $\text{LaTiO}_3/\text{LaAlO}_3$ Multilayers, *Phys. Rev. Lett.* **104**, 036401 (2010).
- [100] N. D. Mermin and H. Wagner, Absence of Ferromagnetism or Antiferromagnetism in One- or Two-Dimensional Isotropic Heisenberg Models, *Phys. Rev. Lett.* **17**, 1133 (1966).
- [101] S. Taniguchi, T. Nishikawa, Y. Yasui, Y. Kobayashi, M. Sato, T. Nishioka, M. Kontani, and K. Sano, Spin gap behavior of $S = 1/2$ quasi-two-dimensional system CaV_4O_9 , *J. Phys. Soc. Jpn.* **64**, 2758 (1995).
- [102] S. Kanungo, S. Kar, and T. Saha-Dasgupta, Tuning of magnetic ground state of the spin- $\frac{1}{2}$ square-lattice compound $\text{Zn}_2\text{VO}(\text{PO}_4)_2$ through chemical substitution, *Phys. Rev. B* **87**, 054431 (2013).
- [103] S. S. Hong, M. Gu, M. Verma, V. Harbola, B. Y. Wang, D. Lu, A. Vailionis, Y. Hikita, R. Pentcheva, J. M. Rondinelli, and H. Y. Hwang, Extreme tensile strain states in $\text{La}_{0.7}\text{Ca}_{0.3}\text{MnO}_3$ membranes, *Science* **368**, 71 (2020).
- [104] A. D. N. James, M. Aichhorn, and J. Laverock, Quantum confinement induced metal-insulator transition in strongly correlated quantum wells of SrVO_3 superlattices, *Phys. Rev. Res.* **3**, 023149 (2021).
- [105] A. D. N. James, E. I. Harris-Lee, A. Hampel, M. Aichhorn, and S. B. Dugdale, Wave functions, electronic localization, and bonding properties for correlated materials beyond the Kohn-Sham formalism, *Phys. Rev. B* **103**, 035106 (2021).
- [106] G. Xing, J. Sun, Y. Li, X. Fan, W. Zheng, and D. J. Singh, Electronic fitness function for screening semiconductors as thermoelectric materials, *Phys. Rev. Materials* **1**, 065405 (2017).
- [107] D. I. Bilc, C. G. Floare, L. P. Zárbo, S. Garabagiu, S. Lemal, and P. Ghosez, First-Principles Modeling of SrTiO_3 Based oxides for thermoelectric applications, *J. Phys. Chem. C* **120**, 25678 (2016).
- [108] T. Okuda, K. Nakanishi, S. Miyasaka, and Y. Tokura, Large thermoelectric response of metallic perovskites: $\text{Sr}_{1-x}\text{La}_x\text{TiO}_3$ ($0 < x < \sim 0.1$), *Phys. Rev. B* **63**, 113104 (2001).
- [109] B. Jalan and S. Stemmer, Large seebeck coefficients and thermoelectric power factor of La-doped SrTiO_3 thin films, *Appl. Phys. Lett.* **97**, 042106 (2010).
- [110] S. Ohta, T. Nomura, H. Ohta, and K. Koumoto, High-temperature carrier transport and thermoelectric properties of heavily La- or Nb-doped SrTiO_3 single crystals, *J. Appl. Phys.* **97**, 034106 (2005).
- [111] H. Ohta, S. Kim, Y. Mune, T. Mizoguchi, K. Nomura, S. Ohta, T. Nomura, Y. Nakanishi, Y. Ikuhara, M. Hirano, H. Hosono, and K. Koumoto, Giant thermoelectric seebeck coefficient of a two-dimensional electron gas in SrTiO_3 , *Nat. Mater.* **6**, 129 (2007).

DuEPublico

Duisburg-Essen Publications online

UNIVERSITÄT
DUISBURG
ESSEN

Offen im Denken

ub | universitäts
bibliothek

This text is made available via DuEPublico, the institutional repository of the University of Duisburg-Essen. This version may eventually differ from another version distributed by a commercial publisher.

DOI: 10.1103/PhysRevResearch.4.033013

URN: urn:nbn:de:hbz:465-20220907-102456-7



This work may be used under a Creative Commons Attribution 4.0 License (CC BY 4.0).